A non-stationary harmonic model for seasonal internal tide amplitude prediction

Matthew D. Rayson, Nicole L. Jones, Gregory N. Ivey, Yankun Gong

[1]Oceans Graduate School and The Oceans Institute, University of Western Australia

Key Points:

- A new empirical model using seasonal harmonics is developed to characterise internal tide variability.
- Seasonal variations in standing internal tides from multiple sources lead to temporal modulations of individual harmonics.
- Internal tide predictability at a site is dependent on standing wave node locations.

Corresponding author: Matthew D. Rayson, matt.rayson@uwa.edu.au

Abstract

We present an empirical model for describing the temporal variability of the internal tide, that uses seasonal harmonics to temporally modulate the amplitude of the fundamental tidal harmonics. Internal tide data, from both long-term, in-situ moorings and a mesoscale- and internal tide-resolving ocean model, are used to demonstrate the performance of the seasonal (non-stationary) harmonic model for the Indo-Australian Basin Region. The non-stationary model described up to 15 % more baroclinic sea surface height and isotherm displacement variance than the fixed-amplitude harmonic model at some observation sites. The ocean model results demonstrate that the study region, which includes the Australian North West Shelf (NWS), Timor Sea and southern Indonesian Islands, is dominated by standing wave interference patterns produced by multiple generation sites. Application of the seasonal harmonic model demonstrates that temporal shifts in the standing wave locations coincide with seasonal variations in density stratification, particularly within 2 - 3 internal wave lengths from strong generation sites. It is shown that the variance fraction of internal tide signal explained by seasonal modulations is largest in standing wave node regions. This result helps explain the contrasting skill of the seasonal harmonic model at two moorings that were separated by only 38 km. Output of the harmonic model also demonstrates that the seasonally-evolving, southward propagating M_2 internal tide from Lombok Strait had a smaller amplitude in October when shear from the Indonesian Throughflow was strongest. Further applications for a regional internal tide climatology database are discussed.

Plain Language Summary

Internal waves drive variability in ocean variables like sea surface height or internal water temperature throughout the ocean. In some regions, most of this variability is centered around the tidal frequencies, i.e., oscillating once or twice per day, due to the surface tides generating the waves. Surface tides are readily predictable using a technique called harmonic analysis due to the mechanical response of the ocean mass to gravitational pull from the Sun and Moon. Internal waves are forced by these tides, however, they are also influenced by temporally variable ocean conditions. Here, we modify the standard harmonic analysis method to account for seasonal variations in ocean properties. For some applications, internal wave-induced variability is considered to be noise

and therefore deterministic methods for describing their variability (the noise) are desirable.

1 Introduction

Prediction of internal tides - internal waves of tidal frequency - is important for numerous practical and ecological applications. Accurate prediction of internal tides is a crucial step in interpreting the future Surface Water Ocean Topography (SWOT) high-resolution altimetry mission and hence obtaining the submesoscale variability (Ray & Zaron, 2011; Arbic et al., 2015). Traditional satellite altimetry is unable to detect internal tide-induced sea surface height (SSH) perturbations over continental shelves because the horizontal wavelength of the barotropic tide is similar to the internal tide wavelength, making their extraction through wavenumber filtering difficult (Zaron, 2019). Horizontal instrument resolution is also a limitation in detecting the shorter internal tides on shelf regions (e.g. Ducet et al., 2000). For example, Zaron (2019)'s internal tide database (high-resolution empirical tide model, or, HRET) predicts internal tide SSH of less than 1 cm in water depths between 200 and 500 m on the Australian North West Shelf (Fig 1) - up to an order of magnitude smaller than observed. Predicting internal tides using other estimates besides altimetry-derived SSH predictions is therefore of critical importance to the interpretation of SWOT SSH data in shelf and coastal zones.

Internal tide prediction techniques largely originate from surface tide methods, namely (stationary) harmonic analysis. Prediction of surface tides is either through empirical harmonic models with fixed tidal frequencies and spatially-varying harmonic amplitudes or response-based models (e.g., Munk & Cartwright, 1966; Foreman, 1977). The harmonic amplitudes are either estimated from tide gauge or satellite altimetry sea surface height data, or from solutions to the shallow-water equations (G. D. Egbert & Ray, 2017). A key characteristic of sites that are not predictable using this approach is that their spectral content exhibit broad "cusps" around each of the forcing frequencies instead of single spectral peaks (Munk & Cartwright, 1966). Broad spectral cusps are usually found in surface tide records where the tides undergo modulations due to low-frequency water level variations (e.g., from storm surge), changing bathymetry or nonlinear effects due to drag.

For internal tide records, broad spectral cusps, centered around the fundamental tidal frequencies forced by the barotropic tide, seem to be the rule rather than the exception (e.g., Colosi & Munk, 2006). The frequency smearing is due to several processes, including temporal variations in stratification and mesoscale flow (Ponte & Klein, 2015; Buijsman et al., 2017; Rainville & Pinkel, 2006; Zaron & Egbert, 2014), and topographic generation through interference from incoming waves (Kelly & Nash, 2010; Gong et al., 2019). Given that they do not form sharp spectral peaks, internal tides are usually defined as the band-passed portion of the signal of an ocean variable like water temperature or buoyancy perturbation (Nash, Kelly, et al., 2012; Buijsman et al., 2017). It is common to name the portion of the band-passed signal that can be modelled with fixed tidal harmonics as the coherent internal tide, and the residual as the incoherent internal tide.

The incoherent internal tide is typically non-stationary and can comprise a significant portion of the total variance in some locations (Shriver et al., 2014; Nelson et al., 2019). It is therefore desirable to model the part of the signal that cannot be explained by fixed tidal frequencies. Zaron (2019) used the approach of Huess and Andersen (2001) to account for seasonal variations in the M_2 internal tide by including an annual modulation, and the non-stationary component is represented in the additional harmonics MA_2 and MB_2. Here we extend this technique to other tidal frequencies and higher harmonics. The purpose of this paper is to demonstrate that part of the non-stationary internal tide variance can be explained using a hierarchical harmonic fitting procedure that accounts for seasonal amplitude modulations of the major tidal constituents (e.g., M_2, S_2, K_1, O_1). We demonstrate the superior performance of this method, compared to the harmonic method, using multi-year in situ mooring observations collected on the Australian North West Shelf (NWS) and Timor Sea, and with a year-long 3D primitive equation ocean model solution encompassing the region.

The NWS, Timor Sea and Indonesian Archipelago are regions where large-amplitude internal tides emanating from different generation sites interact and undergo seasonal modulations (P. Holloway, 2001; Kelly et al., 2014; Robertson & Ffield, 2008; M. Rayson et al., 2012; Gong et al., 2019). Nash, Shroyer, et al. (2012) in their assessment of 16 mooring locations around the globe, found that the most coherent site was in the Timor Sea (ITFTIS). Kelly et al. (2014), showed (by fitting harmonics to 30 day segment lengths) that tidal harmonics at this site underwent annual modulations. They theorised that changes

in seasonal stratification, coherent on the length scale of the wave propagation distance of a few hundred kilometers at this site, were responsible for the annual modulation of the internal tide. We extend the Timor Sea mooring site fixed frequency (stationary) harmonic model by allowing the amplitude of the major tidal harmonics to *slowly* vary in time. We call this approach the non-stationary model as it allows for temporal modulation of the harmonic amplitudes at the primary forcing frequencies (e.g., M_2, K_1). This approach requires specification of a model for the slowly-varying amplitudes, and here we use observations from the Timor Sea mooring to justify using annual harmonics to describe the temporal modulation.

The structure of this paper is as follows. In Section 2, we present the non-stationary harmonic model and define several metrics for characterising the seasonality of internal tides. Descriptions of the in situ data and numerical model setup are given in Section 3. Section 4 begins with an overview of the in situ observations before a quantitative evaluation of the non-stationary harmonic model is presented. We finish Section 4 with a regional overview of the internal tide seasonality using the primitive equation ocean model and explore potential physical drivers in the Discussion in Section 5. We conclude in Section 6 with an overview of potential uses for an internal tide climatology data set and potential modifications to the harmonic model.

2 Non-stationary Harmonic Model

Tidal variations in quantities such as internal wave amplitude, a, are typically modeled using tidal harmonics by employing a series of sinusoidal basis functions with fixed frequencies and amplitudes (cf. Foreman, 1977; G. D. Egbert & Ray, 2017)

$$a_i = \sum_m \alpha_m \cos(\omega_m t_i) + \beta_m \sin(\omega_m t_i) + \varepsilon \,, \tag{1}$$

where ω_m are the tidal harmonic frequencies [cycles d^{-1}], t_i is the time in days at step i, ε is an error term, and α_m and β_m are fixed amplitudes for each harmonic, m. Best estimates of the amplitude parameters are typically found by linear least-squares fitting to the time-series of a_i.

A non-stationary harmonic model is

$$a_i = \sum_m \alpha_{m,i} \cos(\omega_m t_i) + \beta_{m,i} \sin(\omega_m t_i) + \varepsilon_a \,, \tag{2}$$

where the key difference between Eq. 1 and Eq. 2 is that the amplitudes $\alpha_{m,i}$ and $\beta_{m,i}$ now vary with time. This approach, however, results in more unknown variables than data points so the amplitude modulation must be parameterized.

Our non-stationary model allows the amplitudes to vary slowly in time using N seasonal harmonics. With the annual frequency $\omega_A = 2\pi/365.25$ d^{-1}, the real and imaginary amplitudes are now

$$\alpha_{m,i} = \hat{\alpha}_{m,0} + \sum_{n=1}^{N} \hat{\alpha}_{m,n} \cos(n\omega_A t_i) + \hat{\beta}_{m,n} \sin(n\omega_A t_i)\,, \tag{3}$$

and

$$\beta_{m,i} = \tilde{\alpha}_{m,0} + \sum_{n=1}^{N} \tilde{\alpha}_{m,n} \cos(n\omega_A t_i) + \tilde{\beta}_{m,n} \sin(n\omega_A t_i)\,, \tag{4}$$

respectively. The complex time-varying amplitude for any tidal constituent, m, is

$$\hat{\eta}_{m,i} = \alpha_{m,i} + i\beta_{m,i}\,, \tag{5}$$

where $i = \sqrt{-1}$, and will be used throughout this paper to describe the internal tide amplitude variability.

It is possible to estimate the unknown parameters in Eqs. (2) - (4) using linear least-squares methods in two-steps. In the first step, short-time harmonic fits are used to estimate $\alpha_{m,i}$ and $\beta_{m,i}$ for discrete window periods, and in the second step the seasonal harmonic amplitudes (parameters $\hat{\alpha}$ $\hat{\beta}$, $\tilde{\alpha}$ and $\tilde{\beta}$) are least-squares fit to the short-time window amplitude used in step one. The down side of this approach is that one must arbitrarily define a suitable window length. Alternatively, Eqs. (2) - (4) can be combined to give

$$a_t = \sum_{m} \sum_{n=-N}^{N} A_{m,j} \cos([\omega_m + n\omega_A]t_i) + B_{m,j} \sin([\omega_m + n\omega_A]t_i) + \varepsilon_a\,, \tag{6}$$

where the subscript $j = n+N+1$. Eq. 6 highlights how the model captures a broader spectrum of internal waves around each tidal forcing frequency through the additional frequencies given by $\omega_m \pm n\omega_A$.

The unknown parameters which must be estimated from the observed data are the amplitude matrices $A_{m,j}$ and $B_{m,j}$ that have M rows and $2N+1$ columns. For example, with 5 tidal constituents ($M = 5$) and 3 annual harmonics ($N = 3$), $A_{m,j}$ and $B_{m,j}$ each have 35 elements. Last, assuming the error term is zero-mean Gaussian white noise, i.e., $\varepsilon_a \sim \mathcal{N}(0, \sigma_a^2)$, the last parameter to estimate is the standard deviation of the error term, σ_a. The practical benefit of writing the non-stationary model in the form

158 of Eq. 6 is that the parameters can be estimated in one step using linear least-squares
159 fitting. Seasonal modulation of the real and imaginary amplitudes of each tidal harmonic
160 (the terms in Eqs 3 and 4) are then back-calculated from the amplitude matrices in Eq.
161 (6) according to

$$\begin{aligned}
\hat{\alpha}_{m,0} &= A_{m,N+1} \\
\tilde{\alpha}_{m,0} &= B_{m,N+1} \\
\hat{\alpha}_{m,n} &= A_{m,N-n+1} + A_{m,N+n+1} \\
\hat{\beta}_{m,n} &= B_{m,N+n+1} - B_{m,N-n+1} \\
\tilde{\alpha}_{m,n} &= B_{m,N-n+1} + B_{m,N+n+1} \\
\tilde{\beta}_{m,n} &= A_{m,N-n+1} - A_{m,N+n+1}.
\end{aligned} \tag{7}$$

162 Different metrics have been used in the literature to quantify the non-stationarity
163 of internal tides. Shriver et al. (2014) computed tidal fits to 183 30 d segments from 9
164 years of global HyCOM (numerical model) SSH data. They use the normalised RMS of
165 the amplitude for all 183 time blocks as a metric for non-stationarity. In their discus-
166 sion, they also fit annual harmonics to the amplitudes (their Fig. 11). Nash, Shroyer,
167 et al. (2012) used incoherence as a metric for non-stationarity. Their definition for co-
168 herence was the percentage of variance in the 6 - 30 hour band-pass filtered baroclinic
169 current records explained by fitting 8 tidal harmonics to 90 day segments. Ray and Zaron
170 (2011) fit tidal harmonics to altimetry data using data from specific months only to iden-
171 tify seasonality, and hence non-stationarity, of the tidal harmonics.

172 We define the following metrics to characterise the performance and frequency con-
173 tent of the non-stationary harmonic model. The total amount of variance fraction ex-
174 plained by the non-stationary harmonic fit (TVFH) is

$$TVFH = \frac{1}{2}\frac{\sum_{m=1}^{5}\sum_{n=-3}^{3}|\hat{A}_{m,j}|^2}{\langle SSH_{BC}\rangle^2}, \tag{8}$$

175 where $\hat{A}_{m,j} = A_{m,j} + iB_{m,j}$, and $\langle SSH_{BC}\rangle^2$ is the total signal variance. A similar def-
176 inition also applies to the stationary harmonic model, which we call SVFH. These met-
177 rics define the performance of the harmonic model fit and are equivalent to a Murphy
178 Skill score (Murphy, 1988). The variance in an individual frequency band, including an-
179 nual harmonics, is

$$VF_m = \frac{\sum_{n=-3}^{3}|\hat{A}_{m,j}|^2}{\sum_{m=1}^{5}\sum_{n=-3}^{3}|\hat{A}_{m,j}|^2}. \tag{9}$$

The last metric we included is the variance fraction of the non-stationary harmonics for an individual frequency band, defined as

$$NSVF_m = 1 - \frac{|\hat{A}_{m,N+1}|^2}{\sum_{n=-3}^{3} |\hat{A}_{m,j}|^2}. \tag{10}$$

These two metrics (VF_m and $NSVF_m$) explain the dominance of a particular harmonic to the total internal tide signal, and the importance of seasonal modulation to that particular harmonic, respectively.

3 Methods

3.1 *In situ* mooring data

Long time-series of two internal tide ocean quantities, namely the internal mode amplitude, a, and the baroclinic sea surface height perturbation, SSH_{BC}, were extracted from water temperature observations from four vertical moorings deployed in water depths greater than 200 m along the outer region of the Australian North West Shelf and Timor Sea (Fig. 1). Moorings were deployed as part of the Australian Integrated Marine Observing System (IMOS), with the first deployment in February 2012 and the last retrieval in August 2014. Servicing was conducted roughly every six months. Each mooring was equipped with Seabird 37/39/56 thermistors that measured water temperature at 60 s intervals. Instruments were nominally spaced at 20 m depth increments with the uppermost thermistor located 20 - 30 m below mean sea level (Tab. 1). Data from an additional three IMOS moorings that collected TWC temperature data from Aug 2019 - Feb 2020 were used as additional validation data.

3.1.1 Internal tide amplitude estimation

The steps to go from water temperature, $T_{k,i}$ measured with fixed vertical moorings at discrete vertical heights, subscript k, at time interval i, to band-passed internal tide amplitude, a_i, are as follows.

1. Convert temperature to density using a nonlinear equation of state with the climatological mean salinity at each site (34.6 psu).
2. Decompose density into a background component and a perturbation component

$$\rho_{k,i} = \langle \rho \rangle_{k,i} + \rho'_{k,i}$$

where the background component, $\langle\rho\rangle_{k,i}$, is low-pass filtered to remove tidal and higher frequencies (we use a 2-day moving average).

3. Compute the full-water-column background density profile from the discrete data by fitting it to a continuous function

$$\langle\rho\rangle_i(z) = \beta_0 - \beta_1\left[\tanh\left(\frac{z+\beta_2}{\beta_3}\right) + \tanh\left(\frac{z+\beta_4}{\beta_5}\right)\right]$$

4. Calculate the buoyancy frequency, N, and the vertical mode structure functions, ϕ_j for each vertical mode j from the full-water-column background density where

$$N^2(z) = -\frac{g}{\rho_0}\frac{d\langle\rho\rangle}{dz}$$

$g = 9.81$ m s^{-2} is the acceleration due to gravity and $\rho_0 = 1024$ kg m^{-3} is a reference density. The vertical structure functions are then determined from the normal mode eigenvalue equation

$$\frac{d^2\phi_i}{dz^2} + \frac{N_i^2}{c_i^2}\phi = 0 \tag{11}$$

subject to boundary conditions at the top and bottom $\phi(0) = \phi(-H) = 0$, respectively. The eigenvalues, c, are the long-wave phase speed assuming zero rotation.

5. Define buoyancy perturbations as $b(z,\ t) = -g\rho'(z,\ t)/\rho_0$ and solve

$$b(z,\ t) = \sum_{j=1}^{4} A_j(t)N^2(z)\phi_j(z)\,,$$

using least-squares to get a time-series of buoyancy-perturbation amplitude, $A_j(t)$, for each vertical mode.

6. Decompose the amplitude into an internal tide component and a residual

$$A_j(t) = a_j(t) + A'_j(t)$$

where $a_j(t)$ is defined as the band-pass filtered component where we used a Butterworth filter with 6 and 33 hour cutoff periods. It is the internal tide component $a_j(t)$ that we seek to describe with the non-stationary harmonic model.

3.1.2 Baroclinic sea surface height estimation

The internal tide-induced perturbation of the free-surface, the baroclinic sea surface height (SSH_{BC}), is (Zhao et al., 2016)

$$SSH_{BC} = \frac{p_{surf}}{\rho_0 g} \tag{12}$$

where

$$p_{surf} = \rho_0 \int_{-H}^{0} b \; dz \, ,$$

is the surface pressure perturbation, $\rho_0 = 1024$ kg m^{-3} is a constant reference density, H is the water depth, and b is the buoyancy perturbation about the background density i.e.,

$$b = -\frac{(\rho - \langle\rho\rangle)g}{\rho_0}.$$

Note that the definition in Eq. 12 is related to the steric height definition of Savage et al. (2017), but with a few subtle differences. Using our notation, Savage et al. (2017) calculate the steric height η_s from a primitive equation ocean model (HYCOM) via

$$\eta_s = \frac{\overline{\langle\rho\rangle}}{\overline{\rho}}\eta_0 + \frac{\overline{\langle\rho\rangle} - \overline{\rho}}{\overline{\rho}}H$$

where $\overline{()}$ denotes a depth-averaged quantity and η_0 is the initial steric height. Eq. 12 can be re-written in this form to give

$$SSH_{BC} = \frac{\overline{\langle\rho\rangle} - \overline{\rho}}{\rho_0}H.$$

The key points of difference are that we use a reference density in the denominator, assume $\eta_0 = 0$ and use a different definition for the background density $\langle\rho\rangle$. Savage et al. (2017) were interested in the steric height at all frequencies so used a long-term average. Conversely, as we are interested in tidal frequency perturbations to the free-surface, we used a low-pass filter with a cutoff period of 60 hours to give $\langle\rho\rangle$.

3.2 SUNTANS Model

3.2.1 Motivation

A realistic three-dimensional primitive equation ocean solver (described below) was used to model the basin-scale ocean circulation (with tides) for a 12-month period. The purpose of the ocean model was to capture the seasonal variations in large-scale circulation, stratification and their influence on the internal tides. The Indo-Australian basin and the surrounding shelf seas and island chains were investigated in detail; it is one example of many global regions where large scale flow is likely to influence temporal variability of internal tides, which propagate from many different topographic generation regions.

3.2.2 Governing equations

We employ the hydrostatic version of the unstructured grid Stanford University Nonhydrostatic Terrain-following Adaptive Navier-Stokes (SUNTANS) solver (Fringer et al., 2006) to model the ocean circulation. The model solves the Reynolds-averaged Navier-Stokes equations with the Boussinesq and hydrostatic approximations,

$$\frac{\partial u}{\partial t} + \nabla \cdot (\mathbf{u}u) - fv = -g\frac{\partial}{\partial x}(\eta + r) + \nabla_H \cdot (\nu_H \nabla u) + \frac{\partial}{\partial z}\left(\nu_v \frac{\partial u}{\partial z}\right), \tag{13}$$

$$\frac{\partial v}{\partial t} + \nabla \cdot (\mathbf{u}v) + fu = -g\frac{\partial}{\partial y}(\eta + r) + \nabla_H \cdot (\nu_H \nabla v) + \frac{\partial}{\partial z}\left(\nu_v \frac{\partial v}{\partial z}\right), \tag{14}$$

where $\nabla = (\partial/\partial x, \partial/\partial y, \partial/\partial z)$, $\mathbf{u} = (u,\ v,\ w)$ are the eastward, northward and vertical velocity components, respectively, f is the Coriolis frequency, and ν_H and ν_v are the horizontal and vertical eddy viscosity. The free surface elevation is η and r is the baroclinic pressure head given by

$$r = \frac{1}{\rho_0}\int_z^\eta \rho \; dz.$$

where ρ_0 is the reference density (1000 kg˜m^{-3}), and ρ is a perturbation density. The continuity equation is

$$\nabla \cdot \mathbf{u} = 0\,,$$

and the free surface, η, is updated by solving the depth-integrated continuity equation

$$\frac{\partial \eta}{\partial t} + \frac{\partial}{\partial x}\left(\int_{-H}^{\eta} u \; dz\right) + \frac{\partial}{\partial y}\left(\int_{-H}^{\eta} v \; dz\right) = 0.$$

The tracer (temperature and salinity) transport equations are

$$\frac{\partial T}{\partial t} + \nabla \cdot (\mathbf{u}T) = \frac{\partial}{\partial z}\left(K_T \frac{\partial T}{\partial z}\right) + \frac{\partial Q_{sw}}{\partial z}$$

$$\frac{\partial S}{\partial t} + \nabla \cdot (\mathbf{u}S) = \frac{\partial}{\partial z}\left(K_S \frac{\partial S}{\partial z}\right)$$

where T is the temperature [°C], S is the salinity, K_T and K_S are the vertical temperature and salinity diffusivity [m^2 s^{-1}], and Q_{sw} is the penetrative shortwave radiation flux, [°C˜m˜s^{-1}]. A nonlinear equation of state is used to relate density ρ to T, S and pressure [REF].

The model equations are discretized using a hexagonal dominant unstructured horizontal grid (see M. Rayson et al. (2018)) with fixed-height vertical (z-layer) coordinates. See M. D. Rayson et al. (2015) for a thorough overview of the model surface heat, salt and momentum boundary conditions, and Fringer et al. (2006) for an overview of the model discretization and numerical solution method.

3.2.3 Model parameterizations

The surface, $z = \eta(x,\ y,\ t)$, and seabed, $z = -H(x,\ y)$, boundary conditions of the horizontal momentum equations (13, 14) are

$$\nu_v \frac{\partial \mathbf{u}}{\partial z}\bigg|_{z=\eta} = \frac{\vec{\tau}_s}{\rho_0}$$

$$\nu_v \frac{\partial \mathbf{u}}{\partial z}\bigg|_{z=-H} = \frac{\vec{\tau}_b}{\rho_0}$$

where $\vec{\tau}_s = (\tau_{x,s},\ \tau_{y,s})$ and $\vec{\tau}_b = (\tau_{x,b},\ \tau_{y,b})$ are the surface and seabed stress components, respectively. The surface stress is parameterized by

$$\vec{\tau}_s = C_{da}\rho_a \left|\mathbf{U}_a\right| \left(\mathbf{U}_a - \mathbf{u}_{|z=\eta}\right)$$

where ρ_a is the density of air (1.2 kg˜m^{-3}), $\mathbf{U}_a$ is the horizontal wind velocity vector, and C_{da} is the empirical surface drag coefficient. A quadratic drag formulation was also used to define the seabed stress

$$\vec{\tau}_b = -\rho_0 C_d \left|\mathbf{u}_{|z=-H}\right| \mathbf{u}_{|z=-H}.$$

We used a quadratic bed drag coefficient of $C_d = 0.002$. The surface drag coefficient was calculated using the COARE 3.0 algorithm (Fairall et al., 2003), which is wind speed dependent. The horizontal eddy viscosity was constant ($\nu_H = 1.0\ m^2\ s^{-1}$) and the vertical eddy viscosity and tracer diffusivities were computed with the Mellor and Yamada (1982) turbulence closure scheme.

3.2.4 Grid

The model domain encompassed the Australian North West Shelf, Timor Sea and the southern Indonesian Archipelago because these are all known internal wave generation regions. The meridional span of the grid was 23 ° S to 5 ° S and the zonal span was 108° E (west of Western Australia) to 145° E. The easternmost boundary was set to the shallow (20 m) Torres Strait off northern Queensland where there is limited volume exchange with the Coral Sea relative to the Indonesian Throughflow.

SUNTANS uses a finite-volume discretization of the governing equations and therefore employs an unstructured horizontal grid (Fig. 2). We used a hexagonal-dominant

grid that had the finest resolution (roughly 2 km) over the North West Shelf and 4 km resolution in the Timor Sea and the major Indonesian passages of Timor, Ombai and Lombok Straits (Fig 2b). The horizontal resolution telescoped out to about 10 km along all of the open boundaries, coinciding with the resolution of the ocean model used to force the model at the open boundaries (described below). The total number of horizontal grid cells was 225,368. The unstructured grid can therefore efficiently span a large domain with the ability to focus resolution around a region of interest, namely the North West Shelf and the Indonesian-Australian Basin. Grid coordinates were projected in the World Mercator projection (EPSG 54004; https://epsg.io/54004) in order to perform metric distance calculations.

The vertical grid consisted of 80 layers with logarithmic stretching from the surface down to the deepest depth (capped at 6000 m). The vertical resolution was roughly 7 m for the surface layer and each layer thickness increased on the last by a factor of 1.045, giving approximately 20 layers in the upper 250 m and a vertical resolution of roughly 200 m in the abyssal ocean.

A new gridded bathymetry dataset was compiled for the NWS and Indonesian Seas from several data sets using a similar blending method to that described in M. D. Rayson et al. (2017). The input data sets were the Geoscience Australia (GA) 250 m grid from 2009, 50 m resolution multibeam data provided by GA and high-resolution multibeam data provided by Woodside Energy Ltd in selected regions over the NWS. The key difference in this study is that the General Bathymetric Chart of the Oceans (GEBCO) global 30 arc second grid was used in the Indonesian Seas outside of the GA 250 m grid domain. Gridded bathymetry data were interpolated onto the unstructured grid cell centres (Fig. 2a), and the maximum depth was capped at 6000 m.

3.2.5 Model Boundary and Initial Conditions

Background ocean state variables used for the SUNTANS initial and boundary conditions were sourced from the Mercator Ocean global reanalysis product, GLORYSv2. We used daily-average temperature, salinity and velocity variables and interpolated them in space and time onto our model grid points. The GLORYS reanalysis uses the NEMO ocean model with a 1/12th degree resolution global grid and 50 vertical z-levels. The model assimilates satellite sea surface height and temperature data, as well as in situ data from

ARGO profilers, moorings and other sources. It is forced at the ocean surface by the ERA-interim atmospheric reanalysis product (described below).

Barotropic tidal velocity and free-surface boundary conditions were derived from the OTIS China and Indonesian Seas regional tide solution (G. Egbert & Erofeeva, 2002). This regional tide solution has finer grid resolution (1/30°) than the global solution (1/4°) and is therefore able to resolve the Indonesian Archipelago topography in greater detail to provide better tidal predictions (Stammer et al., 2014). Time-varying velocity fluxes and free-surface elevations were reconstructed from eight tidal constituents, namely M_2, S_2, N_2, K_2, K_1, O_1, P_1, Q_1, at the SUNTANS open boundary edges. Tidal fluxes were added to the low-frequency (daily-average) open boundary velocities interpolated from the GLORYS reanalysis.

Atmospheric data from the European Centre for Medium Range Weather Forecast's (ECMWF) ERA-Interim climate reanalysis product was used to drive the exchange of momentum and heat between the atmosphere and the model ocean. ERA-Interim is a global, data-assimilating atmospheric hindcast model run on a roughly 100 km grid with output data stored at six-hourly time steps (Dee et al., 2011). Air-sea fluxes are parameterized in SUNTANS using the COARE3.0 algorithm using east- and north-wind velocity referenced to 10 m above the surface, air temperature, pressure, and relative humidity (Fairall et al., 2003). Net longwave and shortwave radiation components are calculated internally within the model using cloud cover from ERA-Interim and model latitude and time to compute the solar input (see M. D. Rayson et al. (2015) for a description of the numerical implementation of the heat flux module in SUNTANS).

3.3 Validation

We first tested the performance of the ocean model to reproduce the low-frequency evolution of the temperature stratification on the shelf by comparison with through-water-column temperature at the four different shelf locations. Model variables were saved at the observation sites with the same temporal sampling interval (60 seconds). We then linearly interpolated model data onto the observation depths. Temperature bias and RMSE was computed for three different months to evaluate the model performance at capturing the seasonal surface layer and thermocline variations over the region. At the ITFTIS mooring, the model did well at replicating the surface heating and cooling from Septem-

ber 2013 to June 2014, as well as the mixed layer deepening in June (Fig 3). Bias in the upper 100 m was generally close to zero and the RMSE was < 0.5 °C. Model performance was generally worse in the thermocline between 100 and 300 m deep. At the ITFTIS mooring, the model exhibited a 1 - 3 °C warm bias that was most pronounced during June 2014. RMSE was also higher in the thermocline where there were large high-frequency temperature variations due to internal tides. Higher RMSE at these depths were therefore reflective of both mean and internal tide-induced model-data mismatch. Note that as the model was unable to resolve high-frequency, nonlinear internal waves that were present in the observations this also contributed to higher RMSE.

Equivalent model temperature validation plots for the PIL200, KIM400 and KIM200 sites are included in the Supplementary Material. Bias was generally less at the PIL200 and KIM200 shelf sites ($\pm$ 1 ° C), while at the KIM400 site the model exhibited a 1 - 3 °C cool bias in the thermocline between 100 and 300 m. This indicated that there was no systematic temperature bias in the model and that any biases were regionally specific. Poorer validation statistics in the thermocline were due to 20 - 50 m offset in the thermocline depths and admittedly, there is room for improvement in this aspect. Accurately capturing the thermocline structure and strength, however, is an on-going major challenge for all ocean/climate models (e.g., Castaño-Tierno et al., 2018). Overall, the model performed well at capturing the seasonal evolution of near-surface temperature and mixed layer development at each site. It also captured seasonal fluctuations in thermocline strength and width - the main ocean properties likely to temporally modulate internal tides on a regional scale.

4 Results

4.1 Non-stationary internal tides in the Timor Sea

Seasonal variability of the internal tide is exemplified in the SSH_{BC} signal observed at the Timor Sea (ITFTIS) mooring. Short-time harmonic fits of 5 major tidal constituents to 30-day segments over three years revealed seasonal oscillations in the dominant K_1 frequency at the site (Fig. 4a). The K_1 harmonic, in particular, had a strong semi-annual ($2\omega_A$) cycle that could even be noticed in the raw data. Fits of the first three annual harmonics to short time fit harmonic amplitudes are also shown in Fig 4a. These are the slowly-varying real and complex amplitudes ($\alpha_{m,i}$ and $\beta_{m,i}$) in Eqs. 3 and 4. Eq. 6 shows

the relationship between the annual harmonics and the spectral content of the signal. Annual harmonics have an equivalent frequency offset by $\pm n\omega_A$ from each tidal frequency and, since we use $N = 3$ harmonics, there are 6 additional spectral bands per tidal constituent (Fig 4b and c). For example, the semi-annual peak in K_1 amplitude (i.e., $K_1 + 2\omega_A$) was evident in the discrete Fourier transform (DFT) amplitude at ITFTIS where its amplitude was roughly 40 % of the primary frequency (Fig 4b). The semi-diurnal amplitude harmonics were about an order of magnitude smaller than the diurnal harmonics at the ITFTIS and the DFT highlighted that the M_2 band was broadly distributed with amplitude peaks at various annual harmonics (Fig. 4c). Based on this site, we demonstrate the effectiveness of the non-stationary model to capture internal tide seasonal variations. While not all annual harmonics were significant at ITFTIS, their inclusion gives the model suitable flexibility to be broadly applicable to other sites. We will demonstrate the suitability of the approach throughout this paper.

4.2 Non-stationary harmonic model evaluation

We performed the following comparisons of the empirical harmonic models (stationary and non-stationary) using the following in situ variables:

- Mode-1 amplitude at four IMOS moorings (PIL200, KIM200, KIM400, ITFTIS) for a multi-year period (Apr 2012 - Sep 2014);
- SSH_{BC} at the same four IMOS moorings for the 12-month model period (July 2013 - July 2014);
- SSH_{BC} at the same four IMOS moorings for a 12-month period outside of the original numerical model period that was used to estimate the harmonic parameters (July 2012 - July 2013).

We focused on two internal wave-induced ocean state variables to test the harmonic predictions. The first variable was the mode-1 buoyancy perturbation amplitude, and the second was the baroclinic sea surface height. Buoyancy amplitude was chosen as it isolates the signal from individual modes, while SSH_{BC} is a more practical variable because it can be measured from space using altimetry. Note that SSH_{BC} also acts like a filter in that the SSH response is inversely proportional to the vertical mode number so the majority of the signal variance is due to the first baroclinic mode (Zaron 2011). It also allows comparison of our model with other studies which have focused on sea surface height

(e.g., Zhao et al., 2016; Zaron, 2019; Savage et al., 2017; Nelson et al., 2019; Shriver et al., 2014).

We used the non-stationary harmonic amplitudes to characterise the seasonal and geographic variability of different tidal constituents at each site. Following these comparisons, we used the 3D primitive equation solution to make predictions of SSH_{BC} at the mooring locations over the same period when the model was run (July 2013 - June 2014). We then used the ocean model to make predictions at other observational sites collected during different years to the model run period. Last, the ocean model results were used to interpret the seasonal and geographic variability of the in situ observations. Throughout the paper, we use the skill score as a performance evaluation metric

$$skill = 1 - \frac{\sum(X_{mod} - X_{obs})^2}{\sum(X_{obs} - \mu_{obs})^2},$$

where X_{obs} and X_{mod} are the observed and model quantities, respectively, and μ_{obs} is the mean observed quantity.

4.2.1 Mode-1 Amplitude

The total mode-1 amplitude variability, as measured by the standard deviation of raw a for 60-s intervals, was largest at the PIL200 and ITFTIS site (7.1 and 7.3 m, respectively) (Table 2). The standard deviation of KIM400 was roughly half of KIM200, despite the moorings being 38 km apart. This is attributable to the KIM400 mooring being near a standing wave node (e.g., Rayson, 2012), an important result that we will demonstrate later when we show the geographic internal tide variability from the year-long ocean model simulation.

Another feature of the internal wave variability at each of the four sites was that only 20 - 30 % of the amplitude variance was contained within a period range of 6 - 34 hours (broadly encompassing the tidal bands), with the ITFTIS site being the exception with 50 % of the variance contained within these bands. The total variance in the 3 - 34 hour band was much larger (70 - 80 %) at all sites. This larger amount of variance in the super-tidal frequencies at all sites was likely due to the nonlinear steepening of internal tides. Each mooring was located at or near the edge of the continental shelf in water depths of 200 - 500 m, a depth range where the internal tides are known to undergo nonlinear steepening (P. Holloway et al., 1997; Grimshaw et al., 2006; M. D. Rayson et al., 2019).

We tested the suitability of the two empirical harmonic models by comparing the baroclinic mode-1 amplitude, a with the in situ data from four IMOS moorings that were deployed between 2012 and 2014. For the mode-1 amplitude at the ITFTIS and KIM200 sites, the skill of the non-stationary harmonic model was greater at all four sites (Table 3): the non-stationary harmonic model had a skill of 0.78 and 0.81, respectively, while the stationary harmonic model had a skill of 0.66 and 0.70, respectively. The skill of both harmonic models was smallest at KIM400 and PIL200, although the non-stationary model skill was still greater.

4.2.2 Baroclinic SSH

We compared the SSH_{BC} for two time periods. The first was July 2013 - June 2014 and represents the period used to estimate the harmonic amplitude parameters for both the stationary (Eq. 1) and non-stationary (Eq. 6) models; it is therefore a training period. The second period was July 2012 - July 2013 when no data was used to estimate model parameters and hence was a more robust test of the predictive skill of each harmonic model.

The performance of the non-stationary model in predicting a was similar for predicting SSH_{BC} at each of the four sites (Table 4). The non-stationary model had a skill score of 0.88 at ITFTIS compared with 0.78 for the stationary model (Fig. 5). This was the best performing site followed by KIM200 (skill=0.69), PIL200 (skill=0.45) and KIM400 (0.41). The skill score increased and the RMSE reduced at all sites with the non-stationary model, indicating that it is a better performing model, at least for the period containing the data used to estimate the coefficients. The skill at PIL200 and KIM400 showed roughly 50 % improvement by switching to the non-stationary model, suggesting that a larger amount of the variance at the site was explained by the seasonal modulation of the M_2 constituent (discussed below).

To further test the veracity of the non-stationary model, we extrapolated the SSH_{BC} to the period of July 2012 - June 2013 (the previous 12-months of observation data) and calculated the model performance metrics (Table 5). For this period, both the skill and RMSE were similar between the two harmonic models at all sites. For example, at ITFTIS the skill was 0.75 and 0.76 for the stationary and non-stationary model, respectively. This result suggests that the current non-stationary model was less suitable when applied to

a time period outside of the parameter training period, and that inter-annual variability is likely important. However, the data at the ITFTIS site showed that the non-stationary model was qualitatively detecting the semi-annual increase in SSH_{BC} (not shown). There was a slight phase offset and this resulted in a large error for this year of data (July 2012 - June 2013) and this error was reflected in the skill score calculated over 12-months (Table 5). This result of a phase shift in the semi-annual modulation indicates inter-annual variability is likely important, which we have not accounted for at present.

4.2.3 SUNTANS SSH Validation

We tested the ability of the 3D primitive equation ocean model to capture the regional internal tide dynamics by making predictions of SSH_{BC} using the non-stationary harmonic parameters derived from the SUNTANS solution. This enabled a comparison between sites that had concurrent data collection with the model run period (ITFTIS, KIM200, KIM400 and PIL200) and observations collected outside of this period (NWSBAR, NWSROW and NWSBRW moorings). Note that here we are comparing results with the band-passed filtered observation data, not the harmonically-reconstructed observation data. At most sites, the skill score was greater than zero, indicating some predictive capability of the SUNTANS-derived harmonic model (Table 6). The best predictions were (in descending order) the NWSBRW, NWSROW and ITFTIS sites (Skill of 0.67, 0.45 and 0.47, respectively). Note that these were also generally regions of larger total internal tide amplitude (as will be shown below). The poorest predictions were at the KIM400, PIL200 and NWSBAR sites with skill scores of -0.60, 0.02 and 0.12, respectively. These results indicate poorer predictive skill of the non-stationary harmonic model (and SUNTANS) along the southern (Pilbara) section of the NWS.

4.2.4 Seasonal modulation of the internal tide harmonics

Seasonal SSH_{BC} complex harmonic amplitude, $|\hat{\eta}_m(t)|$ (Eq. 5), of the five tidal bands at each of the four sites revealed variable seasonal oscillations in the internal tide harmonics (Fig 6). At ITFTIS (described earlier in Fig. 4), the K_1 and O_1 harmonics had a strong semi-annual cycle although were out of phase; K_1 peaked in July and January while O_1 peaked in November and April (Fig. 6a). The SUNTANS model best reproduced the seasonal variability at the ITFTIS site. The model captured the semi-annual oscillations in the K_1 internal tide ($|\eta_{K1}(t)|$) although was 15 % weaker in magnitude.

Seasonal variations in other constituents at this site were in poorer agreement although all had similar mean amplitudes.

At KIM200 (the next most predictable site), the dominant M_2 harmonic had a tri-annual peak and was largest in August, January and May (Fig 6b). The other four tidal frequencies were all about 25 % or more smaller in magnitude except for K_1, which had tri-annual peaks that were roughly 50 % of the M_2 amplitude. The K_1 tri-annual signal was also apparent in the SUNTANS model although two of the peaks were 50 % weaker. At the nearby KIM400 mooring (38 km away), the M_2 band was at least 25 % of the magnitude of KIM200 and the K_1 internal tide was dominant (Fig. 6c). The K_1 harmonic, however, had a different seasonal structure between the two sites. SUNTANS predicted a dominant M_2 component although K_1 was dominant in the observations (Fig 6c). Again the model under-predicted K_1 by about 50 %. The model was, however, in agreement that the KIM400 semi-diurnal components were significantly weaker than at KIM200.

The seasonal oscillations of the internal tide harmonics exhibited the most complex behaviour at the PIL200 site (Fig. 6d). The M_2 and K_1 bands were dominant although their relative importance varied significantly throughout the year. The M_2 band had tri-annual peaks in July, October and March, while the K_1 band had a semi-annual cycle with peak amplitude in December and July. This resulted in K_1 dominating at PIL200 between October and February and M_2 dominating for the other times of the year. The exception being September, when M_2, N_2 and K_1 were of equal magnitude. The non-stationary harmonic model performed poorest at PIL200, likely the result of transient dynamics not being captured by fitting annual harmonics. At PIL200, the SUNTANS model was in qualitative agreement in terms of the seasonal evolution of the semi-diurnal SSH_{BC} components.

Generally, the SUNTANS derived internal tides were weaker in magnitude when compared to the observed major constituents at all sites. The exception being at KIM400 (Fig 6c). Given the strength of the barotropic tidal forcing was skillfully captured by the model, we suggest that the weaker modeled internal tides were due to a combination of effects: biases in the mean thermocline properties; errors in bathymetry; discretization-induced numerical dissipation due to insufficient horizontal resolution; and too much parameterized dissipation.

4.2.5 Summary of observations

The key insights gained from the empirical harmonic analysis of the in situ mooring data at four locations along the shelf were:

- Internal tide predictability using either fixed amplitude (stationary) harmonics or time-varying (non-stationary) harmonics was best explained at the ITFTIS and KIM200 sites.
- Internal tides at all of the sites were predicted better using the non-stationary harmonic model i.e., accounting for seasonal variability.
- The non-stationary model performed similarly to the stationary model when applied to data from a different time period than that used for harmonic fitting, implying that inter-annual variability of harmonics was also an important factor.
- Internal tide amplitude a was more predictable than SSH_{BC} in terms of skill, probably because a only contains mode-1 contributions.
- ITFTIS was previously shown by (Nash, Shroyer, et al., 2012) to be the most predictable (in terms of a harmonic fit to a 90 day data segment) site of the 16 global shelf moorings investigated. Here we show that the dominant K_1 amplitude has a semi-annual modulation at this site.
- KIM400 had roughly 50 % smaller amplitude internal tides than KIM200 despite being located only 38 km away.
- PIL200 had poor predictability and complicated seasonal variability, such as the dominance of different harmonics throughout the year.

We now use the numerical model results to further explore potential reasons for the geographic variability in seasonal internal tide variability that was observed at these different mooring sites.

4.3 Non-stationarity of internal tides on the NWS

4.3.1 Mean amplitude variability

Spatial variations in the mean M_2 SSH_{BC} amplitude revealed several hot spot regions, including around the major Indonesian Straits (Lombok, Ombai, Timor), on the NWS near Rowley Shoals, and the Browse Basin regions. Furthermore, the model revealed vast regions of standing wave-like characteristics throughout the domain, includ-

ing on the shelf between the 200 and 500 m isobaths (Fig 7a). The standing wave patterns led to nodes and anti-nodes in SSH_{BC} that varied over spatial scales of roughly one internal tide wave length (roughly 50 km on the shelf and 100 km in the deep basin).

Qualitatively, this agreed with the spatial variations from the altimetry-derived HRET model (Fig 1). Some obvious differences between the HRET and the SUNTANS-derived harmonic amplitudes were close to islands (e.g. Lombok Strait) and on the NWS in depths less than 500 m. A known limitation of the satellite-filtering process is the necessity to filter out signals in shallow water where the internal tides and barotropic tides vary over similar length scales (e.g. Zaron 2019). The K_1 component, which was dominant in the Timor Sea but weak on the North West Shelf, also formed standing internal tide patterns (Fig. 7b). It was also significantly larger than the K_1 amplitude from the HRET (not shown).

4.3.2 Regional variability of non-stationary metrics

The non-stationary model was a far more suitable descriptor of the SSH_{BC} from the 12-month model simulation in terms of the difference between TVFH and SVFH (Fig 8). On the shelf/ slope region (200 - 500 m), where all of the mooring sites examined here were located, the TVFH parameter exceeded 50 % and was always greater than SVFH (Table 7). In large parts of the Timor Sea and Browse Basin regions the TVFH exceeded 90 % (Fig 8a). Of note, is that TVFH was consistently lower in nodal regions (described below) such as the KIM400 mooring site. This site had lower overall signal variance and this analysis reveals that the signal is comprised of greater variability at other frequencies or undergoes more severe amplitude modulation. PIL200 also appeared to straddle a standing internal wave node point.

The variance fraction of the harmonic signals in the M_2 and K_1 bands (VF_m) closely resembled the mean harmonic amplitude with M_2 dominance (60 - 90 % of variance) on the NWS and throughout the Indo-Australian basin (Fig 9a). Conversely, the VF_{K1} was dominant in the Timor Sea. There were, however, isolated patches where this general picture was violated. A notable example was the prevalence of the K_1 band around PIL200 where VF_{K1} was roughly 50 % (VF_{M2} and VF_{K1} were 43 and 23 %, respectively Table 7). Likewise, there were regions of the Timor Sea, away from ITFTIS, where $VF_{M2} >$ 50 %, whereas VF_{M2} was only 2 % at ITFTIS. These isolated patches emphasise why

individual moorings may not be representative of the wider regional variability of internal tide-induced sea level fluctuations.

The non-stationary variance fraction ($NSVF_m$) generally peaked in standing wave node regions for both the M_2 and K_1 bands (Fig. 10). There were only large spatial regions of non-stationary variance on the shelf in water depths less than 200 m where seasonal variations in mixed layer depth led to no stratification, and no internal waves, and a mean amplitude close to zero (see Fig. 7). The less predictable mooring sites (in terms of the non-stationary model skill score in Table 6) also exhibited greater $NSVF_{M2}$ e.g., it was 59 % at PIL200 and 40 % at KIM400 (Table 7).

4.3.3 Temporal evolution of standing internal tides

The ITFTIS mooring was situated in the center of an anti-node, explaining the strong K_1 signal at the site. Seasonal variations in $|\eta_{K1}|$ at the site, however, did not appear to be due to spatial shifting of these standing wave regions but rather due to changes in total amplitude (Fig 11). During October, when the mixed layer was relatively deep in the Timor Sea, $|\eta_{K1}|$ was at a minimum, whereas during January, when there was near-surface stratification, the amplitude peaked.

The node/anti-node variation is the main reason why the KIM200 and KIM400 have such a different internal tide variability despite being relatively close in space. The KIM400 mooring was located in an M_2 node region throughout the year (Fig 12), whereas the KIM200 was in a node for part of the year (e.g. October), but in an anti-node during January. Note that the baroclinic velocity will have the opposite response to SSH_{BC} and isotherm displacement amplitude; velocity will peak in the SSH_{BC} nodes and be smallest in the anti-nodes see e.g. M. Rayson et al. (2012),.

4.3.4 Summary of model results

The key results from the 12-month ocean model non-stationary harmonic fit were:

- Internal tide amplitudes in all frequency bands exhibited standing wave patterns;
- Predictability at a given observation point generally coincided with the location of nodes and anti-nodes and also with the total signal variance fraction in the seasonal harmonics;

- The ability of both the non-stationary and stationary empirical harmonic models to capture the total SSH_{BC} signal variance was regionally-dependent, with the Timor Sea being the most predictable and the Pilbara region (southern NWS) being the least predictable.
- Overall, the non-stationary model captured more of the signal variance, as it includes 7 times more frequencies and hence amplitude parameters than the stationary model.
- In regions where the harmonic fit described zero percent of the variance, like on the shelf in water shallower than 200 m, a non-stationary fit is essential.

5 Discussion

Non-stationary internal tides are primarily believed to be caused by perturbations in the internal wave phase speed due to time-variable stratification, mean flow and relative vorticity (Zaron & Egbert, 2014). In a two-dimensional wave field, phase speed perturbations will cause shifts in the location of constructive and destructive interference, thus driving variability over length scales of less than one wave length (50 - 150 km). The dominant mesoscale flow feature in the NE Indian Ocean is the strong Indonesian Throughflow (ITF) that persistently flows in a westerly direction from roughly June to December (Meyers et al., 1995). This flow breaks down into a series of eddies (instabilities) between December and March when the northern Australian monsoon winds shift from south easterly to northwesterly (Feng & Wijffels, 2002). Monthly-averaged steric height SSH and surface currents from the internal-tide resolving SUNTANS model exhibited these features. In particular, a N-S SSH gradient and strong westward surface flow around October 2013 (Fig. 13a). Whereas by January 2013, the mean N-S SSH gradient had relaxed and was replaced by a series of geostrophically-balanced mesoscale eddies (Fig. 13b). The mode-1 linear phase speed, (Zhao et al., 2016)

$$c_1 = \frac{\omega}{(\omega^2 - f^2)^{1/2}} c$$

where f is the Coriolis frequency and c is given by Eq. 11, was calculated using changes in background stratification only. The phase speed was up to 0.3 m s^{-1} faster in the *austral* summer compared with spring (February minus October) over the NWS and south of Indonesia (Fig. 13c). In the deeper regions of the Indo-Australian Basin, the phase speed difference was roughly 0.1 m s^{-1} slower, although this was in a region where the total phase speed was greater than 3.0 m s^{-1}.

To identify the temporal modulation of the internal tide amplitude between Indonesia and the NWS due to refraction and/or Doppler-shifting, we interpolated $|\eta_{M2}(t)|$ along a line between Lombok Strait and the Rowley Shoals (transect line shown in Fig. 13c). Seasonal variation in $|\eta_{M2}(t)|$ was evident at each location along the transect; for example, along 10.5 °S there were two major peaks in $|\eta_{M2}(t)|$, one in January and one in June 2014. Conversely, along 11 °S there was a single peak around February 2014. These differences in seasonal peaks over such short distances can partly be explained by variations in arrival time due to changes in phase speed (Fig 14b). By assuming for simplicity that wave propagation is one-dimensional, we calculated the propagation time, $\tau(y,t)$, from the time-varying phase speed along the transect line using

$$\tau(y,t) = \int_0^y \frac{1}{c_1(y',t)} dy' \,,$$

where y is the distance along the transect line. Contours of $\tau(y,t)$ help identify the drivers of spatial differences in $|\eta_{M2}(t)|$ due to stratification-induced refraction (black contours on Fig. 14). The peak in $|\eta_{M2}(t)|$ at 11 °S during March 2014 corresponded with a period when the line of constant propagation time migrated further south due to the increased phase speed south of Lombok Strait. Lines of constant propagation time were less indicative of amplitude modulations further from the primary internal tide source regions, e.g., between 12 and 16 °S in Fig. 14a. This discrepancy is likely due to other processes causing perturbations in the mode-1 phase speed (namely the mean flow and vorticity), and also due to the wave propagation being two-dimensional.

Doppler-shifting of the internal tide harmonics may be inferred using the present analysis by finding time periods when the signal amplitude was reduced. To calculate two-dimensional variations in amplitude reduction, we performed a directional decomposition of the complex harmonic amplitudes using the technique outlined in Gong et al. (2020). This technique takes a 2D Fourier transform of the complex spatial internal tide amplitude, filters the horizontal wavenumbers (that are both positive and negative) according to a directional band of choice, and then takes the inverse Fourier transform. The SE propagating component (filter band of 0 to 90 degrees CCW from E) isolated the internal tide originating from Indonesia, while the NW propagating component isolated the NWS-generated internal tide (Fig 15). Temporal modulations of the SE component were most pronounced in the centre of the Indo-Australian basin and on the NWS slope. The modulating component on the NWS was evident in the multi-directional signal (e.g. Fig 10), and is described in detail in (M. Rayson et al., 2012). Between 8 and

14 ° S, the SE propagating component, which originated near Lombok strait, was 1 - 2 cm (50 % or more) smaller during October than it was during February (Fig 15d-f). Likewise, the NW propagating component, which originated along the NWS, was 1 - 2 cm smaller near Indonesia during October than it was in February (Fig 15a-c). We attribute the amplitude reduction in SSH_{BC} around October to Doppler shifting of the low-mode internal tide caused by the strong ITF flow during this period (e.g. Fig. 13a). Energy fluxes from internal waves into the background mean flow are also likely to cause some of the amplitude variations (e.g., Dunphy & Lamb, 2014).

A conventional view of internal tides at a fixed site, like a mooring, is that the local barotropic forcing frequency will directly transfer into the frequency content of the internal motions. Multiple generation sites and long propagation distances, however, lead to high spatial variability of internal wave-induced ocean scalars (i.e., decorrelation length scales of less than one internal tide wave length). For example, despite the M_2 barotropic tide being dominant on the NWS (P. E. Holloway, 1983), the KIM200 mooring was the only site where the M_2 baroclinic component was dominant throughout the year (see Fig. 6). This is contrary to the conventional view that the M_2 internal tide is dominant (e.g., P. Holloway, 2001; M. Rayson et al., 2012; Kelly et al., 2014). While this conventional picture was generally true in the numerical model solution (see e.g., Fig. 7), the results presented here indicate that large spatial variations in amplitude occur over short distances of generally less than one wave length. Conversely in the Timor Sea, there is a M_2 tidal amphidrome resulting in the dominance of diurnal barotropic tides (see e.g., Robertson and Ffield (2008)). Based on an analysis of the ITFTIS mooring it may be tempting to conclude that the K_1 internal tide is therefore also dominant in the Timor Sea. The regional internal tide model highlighted, however, that there are regions within 30 km of the mooring where the M_2 component is dominant (Fig. 9a), likely due to remotely generated internal tides. The high spatial variability is an important consideration to take into account when choosing mooring field sampling strategies to study the internal tide (or in trying to interpret data from a mooring). Finally, we have not presented any analysis of internal tide-induced velocity perturbations. It should be noted that in places where standing internal waves are dominant (almost everywhere in this domain), regions of small SSH_{BC} or isotherm displacement amplitude variance will likely have large baroclinic velocity variance. Interpretation of individual and isolated in situ

observations requires knowledge of the broader spatial context, namely the regional internal tide interference patterns.

6 Conclusions

A key output of harmonically-decomposing internal tide amplitude or SSH_{BC} from primitive equation ocean model solutions, like our one-year SUNTANS solution for the Indo-Australian Basin, is an internal tide climatological database. By including the "seasonal sidelines" in our harmonic analysis, as hinted at in Arbic et al. (2015), we have shown that a greater amount of internal tide variance is captured, particularly around shelf regions (see e.g., Fig. 8, Tab. 4). This climatology has practical applications including: allowing the removal of internal tide signals for future satellite altimetry missions (e.g., Morrow et al., 2019); or in supplying boundary conditions for regional internal wave modelling applications (e.g., Gong et al., 2020). Here we have constructed a regional internal tide database and a global database that could readily be calculated using output from a global internal-tide resolving model, e.g., the 1/25° HyCOM model in Savage et al. (2017) or the 1/48° LLC4320 MITGCM run in Torres et al. (2018).

Various studies, including this one, have demonstrated that tidal harmonics are a useful description of internal tide variability when applied over short time periods (generally less than a month). The most important aspect of internal tide prediction is how to model the temporal modulation of these short time window amplitudes. Here, we used a seasonal harmonic model that was motivated by the modulation of the Timor Sea internal tides, which are primarily driven by seasonal changes in the ocean stratification (Kelly et al., 2014). This seasonal model is less suited to other regions of the globe (the PIL200 site is one example) where internal tide variations are due to more transient (aperiodic) features like mesoscale eddies. To model the temporal modulation in these regions, non-parametric techniques, like splines or Gaussian processes, are likely to be better suited. These methods, however, rely on having recent data to make predictions of internal tides into the short future i.e. so-called data-driven statistical techniques. In regions where internal tide prediction is important for operational decision making, these data-driven techniques will be necessary. Our parametric seasonal harmonics provided a better prediction of the internal tides throughout most of the study region and therefore are a useful starting point for these more data-intensive statistical modelling techniques.

Acknowledgments

This work was supported by the Australian Research Council Industrial Transformation Research Hub for Offshore Floating Facilities (IH140100012). This work was supported by resources provided by the Pawsey Supercomputing Centre with funding from the Australian Government and the Government of Western Australia. Observation data was sourced from Australia's Integrated Marine Observing System (IMOS) — IMOS is enabled by the National Collaborative Research Infrastructure strategy (NCRIS). Quality controlled observation data is available on the Australian Ocean Data Network (https://portal.aodn.org.au). Numerical model tide data is available at: tpxo.net/regional. Initial and boundary condition data are at (https://resources.marine.copernicus.eu/documents/PUM/CMEMS-GLO-PUM-001-030.pdf). Processed numerical model output and observation data are archived on the UWA library research repository (https://doi.org/10.26182/8jx9-m532).

References

Arbic, B. K., Lyard, F., Ponte, A., Ray, R. D., Richman, J. G., Shriver, J. F., ... Zhao, Z. (2015). Tides and the SWOT mission: Transition from Science Definition Team to Science Team. (January), 1–8.

Buijsman, M. C., Arbic, B. K., Richman, J. G., Shriver, J. F., Wallcraft, A. J., & Zamudio, L. (2017, 7). Semidiurnal internal tide incoherence in the equatorial Pacific. *Journal of Geophysical Research: Oceans*, *122*(7), 5286–5305. Retrieved from `https://onlinelibrary.wiley.com/doi/abs/10.1002/2016JC012590` doi: 10.1002/2016JC012590

Castaño-Tierno, A., Mohino, E., Rodríguez-Fonseca, B., & Losada, T. (2018). Revisiting the CMIP5 Thermocline in the Equatorial Pacific and Atlantic Oceans. *Geophysical Research Letters*, *45*(23), 963–12. doi: 10.1029/2018GL079847

Colosi, J. A., & Munk, W. (2006). Tales of the venerable Honolulu tide gauge. *Journal of Physical Oceanography*, *36*(6), 967–996. doi: 10.1175/JPO2876.1

Dee, D. P., Uppala, S. M., Simmons, A. J., Berrisford, P., Poli, P., Kobayashi, S., ... Vitart, F. (2011). The ERA-Interim reanalysis: Configuration and performance of the data assimilation system. *Quarterly Journal of the Royal Meteorological Society*, *137*(656), 553–597. doi: 10.1002/qj.828

Ducet, N., Le Traon, P. Y., & Reverdin, G. (2000). Global high-resolution mapping of ocean circulation from TOPEX/Poseidon and ERS-1 and -

2. *Journal of Geophysical Research: Oceans*, *105*(C8), 19477–19498. doi: 10.1029/2000jc900063

Dunphy, M., & Lamb, K. G. (2014). Focusing and vertical mode scattering of the first mode internal tide by mesoscale eddy interaction. *Journal of Geophysical Research: Oceans*, *119*(1), 523–536. doi: 10.1002/2013JC009293

Egbert, G., & Erofeeva, S. (2002). Efficient inverse modeling of barotropic ocean tides. *Journal of Atmospheric & Oceanic Tec hnology*, 183–204. Retrieved from `http://search.ebscohost.com/login.aspx?direct=true&profile=ehost&scope=site&authtype=crawler&jrnl=07390572&AN=5921008&h=7UU9nfXl%2BWu2UVAMNCDBGMUYLT1OaMoBFeNs0sLOwG%2Fx0NLEHdBqyaMiw4E2%2BgjPDBSm2lrWDilU6meYSmzttA%3D%3D&crl=c`

Egbert, G. D., & Ray, R. D. (2017). Tidal prediction. *Journal of Marine Research*, *75*(3), 189–237. doi: 10.1357/002224017821836761

Fairall, C. W., Bradley, E. F., Hare, J. E., Grachev, A. A., & Edson, J. B. (2003). Bulk parameterization of air-sea fluxes: Updates and verification for the COARE algorithm. *Journal of Climate*, *16*(4), 571–591. doi: 10.1175/1520-0442(2003)016⟨0571:BPOASF⟩2.0.CO;2

Feng, M., & Wijffels, S. (2002). Intraseasonal variability in the SEC of the East Indian ocean. *J. Phys. Oceanogr.*, *32*, 265–277.

Foreman, M. G. G. (1977). *Manual for tidal heights analysis and prediction* (Tech. Rep.). Institute of Ocean Sciences, Patricia Bay.

Fringer, O. B., Gerritsen, M., & Street, R. L. (2006). An unstructured-grid, finite-volume, nonhydrostatic, parallel coastal ocean simulator. *Ocean Modelling*, *14*(3-4), 139–173. doi: 10.1016/j.ocemod.2006.03.006

Gong, Y., Rayson, M. D., Jones, N. L., & Iver, G. N. (2020). Directional decomposition of internal tides propagating from multiple generation sites. *under review in Ocean Modelling*.

Gong, Y., Rayson, M. D., Jones, N. L., & Ivey, G. N. (2019). The Effects of Remote Internal Tides on Continental Slope Internal Tide Generation. *Journal of Physical Oceanography*, *49*(6), 1651–1668. doi: 10.1175/jpo-d-18-0180.1

Grimshaw, R., Pelinovsky, E., Stepanyants, Y., & Talipova, T. (2006). Modelling internal solitary waves on the Australian North West Shelf. *Marine and Freshwater Research*, *57*(3), 265. doi: 10.1071/mf05016

Holloway, P. (2001). A regional model of the semidiurnal internal tide on the Australian North West Shelf. *Journal of Geophysical Research: Oceans (1978 ...*, *106*. Retrieved from http://onlinelibrary.wiley.com/doi/10.1029/2000JC000675/full

Holloway, P., Pelinovsky, E., Talipova, T., & Barnes, B. (1997). A nonlinear model of internal tide transformation on the Australian North West Shelf. *Journal of Physical*, *27*, 871–896. Retrieved from http://journals.ametsoc.org/doi/pdf/10.1175/1520-0485(1997)027%3C0871:ANMOIT%3E2.0.CO;2

Holloway, P. E. (1983). *Tides on the australian north-west shelf* (Vol. 34) (No. 1). doi: 10.1071/MF9830213

Huess, V., & Andersen, O. B. (2001). Seasonal variation in the main tidal constituent from Altimetry. *Geophysical Research Letters*, *28*(4), 567–570. doi: 10.1029/2000GL011921

Kelly, S. M., Jones, N. L., Ivey, G. N., & Lowe, R. J. (2014). Internal-Tide Spectroscopy and Prediction in the Timor Sea. *Journal of Physical Oceanography*, *45*(1), 64–83. Retrieved from http://dx.doi.org/10.1175/JPO-D-14-0007.1 doi: 10.1175/JPO-D-14-0007.1

Kelly, S. M., & Nash, J. D. (2010, 12). Internal-tide generation and destruction by shoaling internal tides. *Geophysical Research Letters*, *37*(23), n/a-n/a. Retrieved from http://doi.wiley.com/10.1029/2010GL045598 doi: 10.1029/2010GL045598

Mellor, G., & Yamada, T. (1982). Development of a Turbulence Closure Model for Geophysical Fluid Problems. *Reviews of Geophysics and Space Physics*, *20*(4), 851–875.

Meyers, G., Bailey, R. J., & Worby, A. P. (1995). Geostrophic transport of Indonesian throughflow. *Deep-Sea Research Part I*, *42*(7), 1163–1174. doi: 10.1016/0967-0637(95)00037-7

Morrow, R., Fu, L. L., Ardhuin, F., Benkiran, M., Chapron, B., Cosme, E., ... Zaron, E. (2019). Global observations of fine-scale ocean surface topography with the Surface Water and Ocean Topography (SWOT) Mission. *Frontiers in Marine Science*, *6*(APR), 1–19. doi: 10.3389/fmars.2019.00232

Munk, W. H., & Cartwright, D. (1966). TIDAL SPECTROSCOPY AND PREDICTION. *PHILOSOPHICAL TRANSACTIONS OF THE ROYAL SOCIETY*

OF LONDON, *259*(1105), 533–581. doi: 10.2307/j.ctt211qv60.7

Murphy, A. (1988). Skill scores based on the mean square error and their relationships to the correlation coefficient. *Monthly weather review*. Retrieved from http://journals.ametsoc.org/doi/abs/10.1175/1520-0493(1988)116%3C2417:SSBOTM%3E2.0.CO%3B2

Nash, J. D., Kelly, S. M., Shroyer, E. L., Moum, J. N., & Duda, T. F. (2012). The unpredictable nature of internal tides on continental shelves. *Journal of Physical Oceanography*, *42*(11), 1981–2000. doi: 10.1175/JPO-D-12-028.1

Nash, J. D., Shroyer, E., Kelly, S., Inall, M., Duda, T., Levine, M., ... Musgrave, R. (2012, 6). Are Any Coastal Internal Tides Predictable? *Oceanography*, *25*(2), 80–95. Retrieved from http://dx.doi.org/10.5670/oceanog.2012.44https://tos.org/oceanography/article/are-any-coastal-internal-tides-predictable doi: 10.5670/oceanog.2012.44

Nelson, A. D., Arbic, B. K., Zaron, E. D., Savage, A. C., Richman, J. G., Buijsman, M. C., & Shriver, J. F. (2019). Toward Realistic Nonstationarity of Semidiurnal Baroclinic Tides in a Hydrodynamic Model. *Journal of Geophysical Research: Oceans*, *124*(9), 6632–6642. doi: 10.1029/2018JC014737

Ponte, A. L., & Klein, P. (2015). Incoherent signature of internal tides on sea level in idealized numerical simulations. *Geophysical Research Letters*, *42*(5), 1520–1526. doi: 10.1002/2014GL062583

Rainville, L., & Pinkel, R. (2006). Propagation of low-mode internal waves through the ocean. *Journal of Physical Oceanography*, *36*(6), 1220–1236. doi: 10.1175/JPO2889.1

Ray, R. D., & Zaron, E. D. (2011). Non-stationary internal tides observed with satellite altimetry. *Geophysical Research Letters*, *38*(17), 1–5. doi: 10.1029/2011GL048617

Rayson, M., Ivey, G., Jones, N., & Fringer, O. (2018). Resolving high-frequency internal waves generated at an isolated coral atoll using an unstructured grid ocean model. *Ocean Modelling*, *122*. doi: 10.1016/j.ocemod.2017.12.007

Rayson, M., Jones, N., & Ivey, G. (2012). Temporal variability of the standing internal tide in the Browse Basin, Western Australia. *Journal of Geophysical Research: Oceans*, *117*(6). doi: 10.1029/2011JC007523

Rayson, M. D., Gross, E. S., & Fringer, O. B. (2015, 5). Modeling the tidal and sub-

tidal hydrodynamics in a shallow, micro-tidal estuary. *Ocean Modelling*, *89*, 29–44. Retrieved from https://linkinghub.elsevier.com/retrieve/pii/S1463500315000207 doi: 10.1016/j.ocemod.2015.02.002

Rayson, M. D., Ivey, G. N., Jones, N. L., & Fringer, O. B. (2017). Scott Reef SUNTANS Hydrodynamic Modelling Study. , 1–208.

Rayson, M. D., Jones, N. L., & Ivey, G. N. (2019). Observations of Large-Amplitude Mode-2 Nonlinear Internal Waves on the Australian North West Shelf. *Journal of Physical Oceanography*, *49*(1), 309–328. doi: 10.1175/jpo-d-18-0097.1

Robertson, R., & Ffield, A. (2008). Baroclinic tides in the Indonesian seas: Tidal fields and comparisons to observations. *Journal of Geophysical Research: Oceans*, *113*(7), 1–22. doi: 10.1029/2007JC004677

Savage, A. C., Arbic, B. K., Richman, J. G., Shriver, J. F., Alford, M. H., Buijsman, M. C., ... Zamudio, L. (2017, 3). Frequency content of sea surface height variability from internal gravity waves to mesoscale eddies. *Journal of Geophysical Research: Oceans*, *122*(3), 2519–2538. Retrieved from http://doi.wiley.com/10.1002/2016JC012331 doi: 10.1002/2016JC012331

Shriver, J. F., Richman, J. G., & Arbic, B. K. (2014, 5). How stationary are the internal tides in a high-resolution global ocean circulation model? *Journal of Geophysical Research: Oceans*, *119*(5), 2769–2787. Retrieved from http://doi.wiley.com/10.1002/2013JC009423 doi: 10.1002/2013JC009423

Stammer, D., Ray, R. D., Andersen, O. B., Arbic, B. K., Bosch, W., Carrère, L., ... Yi, Y. (2014, 9). Accuracy assessment of global barotropic ocean tide models. *Reviews of Geophysics*, *52*(3), 243–282. Retrieved from http://doi.wiley.com/10.1002/2014RG000450 doi: 10.1002/2014RG000450

Torres, H. S., Klein, P., Menemenlis, D., Qiu, B., Su, Z., Wang, J., ... Fu, L. L. (2018). Partitioning Ocean Motions Into Balanced Motions and Internal Gravity Waves: A Modeling Study in Anticipation of Future Space Missions. *Journal of Geophysical Research: Oceans*, *123*(11), 8084–8105. doi: 10.1029/2018JC014438

Zaron, E. D. (2019). Baroclinic tidal sea level from exact-repeat mission altimetry. *Journal of Physical Oceanography*, *49*(1), 193–210. doi: 10.1175/JPO-D-18-0127.1

Zaron, E. D., & Egbert, G. D. (2014). Time-Variable Refraction of the Internal

926 Tide at the Hawaiian Ridge. *Journal of Physical Oceanography*, *44*(2), 538–
927 557. Retrieved from http://journals.ametsoc.org/doi/abs/10.1175/
928 JPO-D-12-0238.1 doi: 10.1175/JPO-D-12-0238.1
929 Zhao, Z., Alford, M. H., Girton, J. B., Rainville, L., & Simmons, H. L. (2016).
930 Global Observations of Open-Ocean Mode-1 M ¡sub¿2¡/sub¿ Internal Tides.
931 *Journal of Physical Oceanography*, *46*(6), 1657–1684. Retrieved from
932 http://journals.ametsoc.org/doi/10.1175/JPO-D-15-0105.1 doi:
933 10.1175/JPO-D-15-0105.1

FIGURES

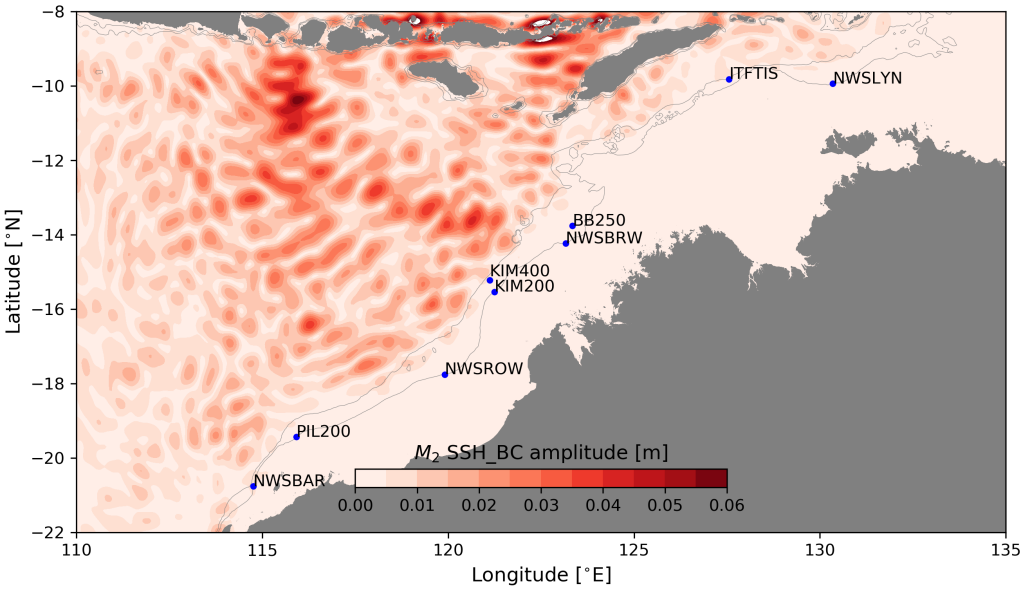

Figure 1. Map of the field sites with the M_2 baroclinic sea surface height amplitude [m] from Zaron (2019) overlaid. Grey lines indicate the 200 and 500 m depth contours that highlight the edge of the continental shelf.

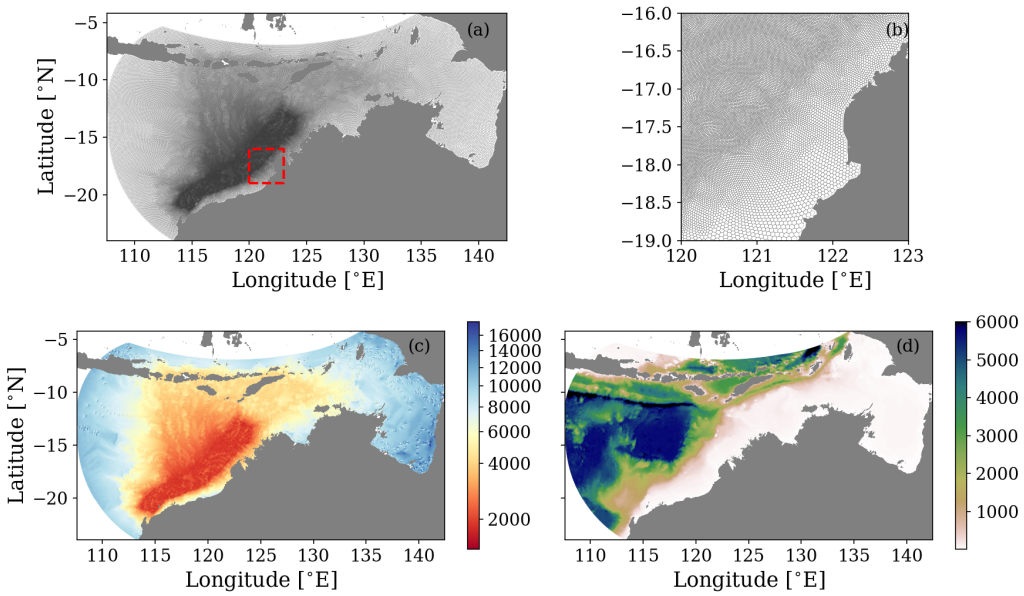

Figure 2. (a,b) Unstructured hexagonal-dominant SUNTANS mesh encompassing the Indo-Australian Basin, North West Shelf, Timor Sea and Gulf of Carpentaria. (c) Horizontal grid resolution [m] noting that colours are on a nonlinear scale and (d) model bathymetry [m].

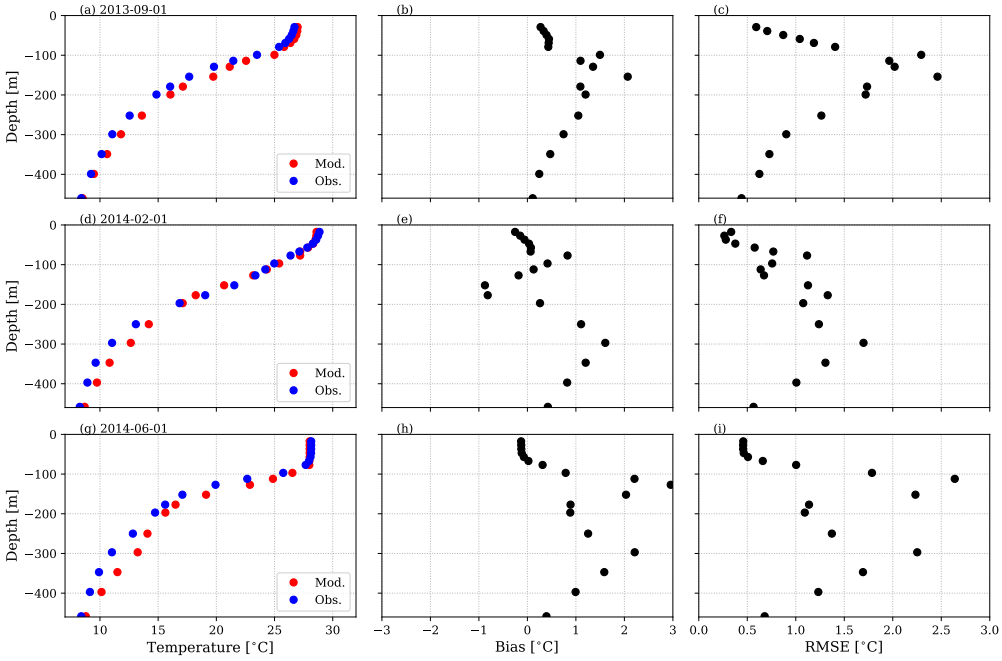

Figure 3. Quantitative SUNTANS model evaluation metrics against in situ temperature observations from the ITFTIS mooring of (left column) monthly-averaged temperature, (middle column) temperature bias, and (right column) temperature root mean square error. Each row corresponds with monthly-averages for September 2013, February 2014 and June 2014.

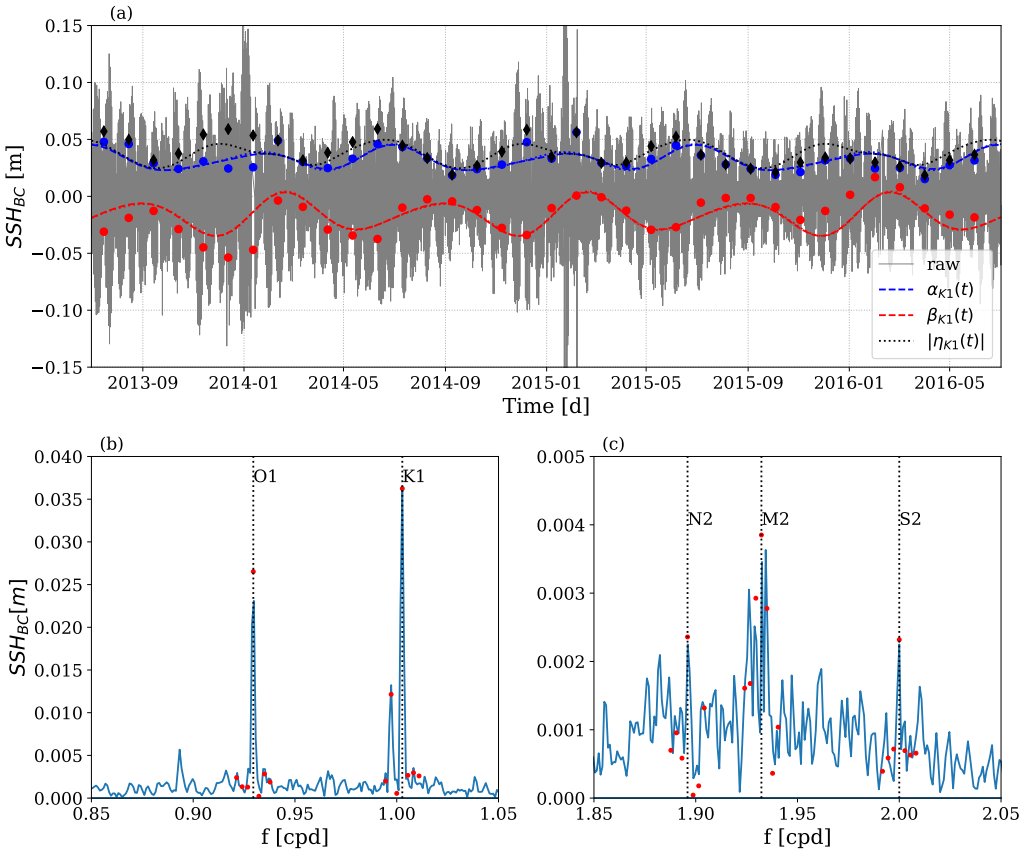

Figure 4. (a) 3-year time series of baroclinic sea surface height [m] at the Timor Sea (ITFTIS) mooring. Blue and red dots indicate the real and imaginary K_1 amplitudes, respectively, from harmonic fitting 30 d segments, while the black dots indicate the complex amplitude magnitude. The dashed lines indicate the seasonal harmonic model fit to the discrete amplitudes. (b) and (c) are the discrete Fourier transform amplitude for the diurnal and semidiurnal bands, respectively (note the change in vertical scale). Red dots in (b) and (c) indicate the least-squares fit amplitude of the tidal bands plus the annual harmonics.Note the different vertical scales in (b) and (c)

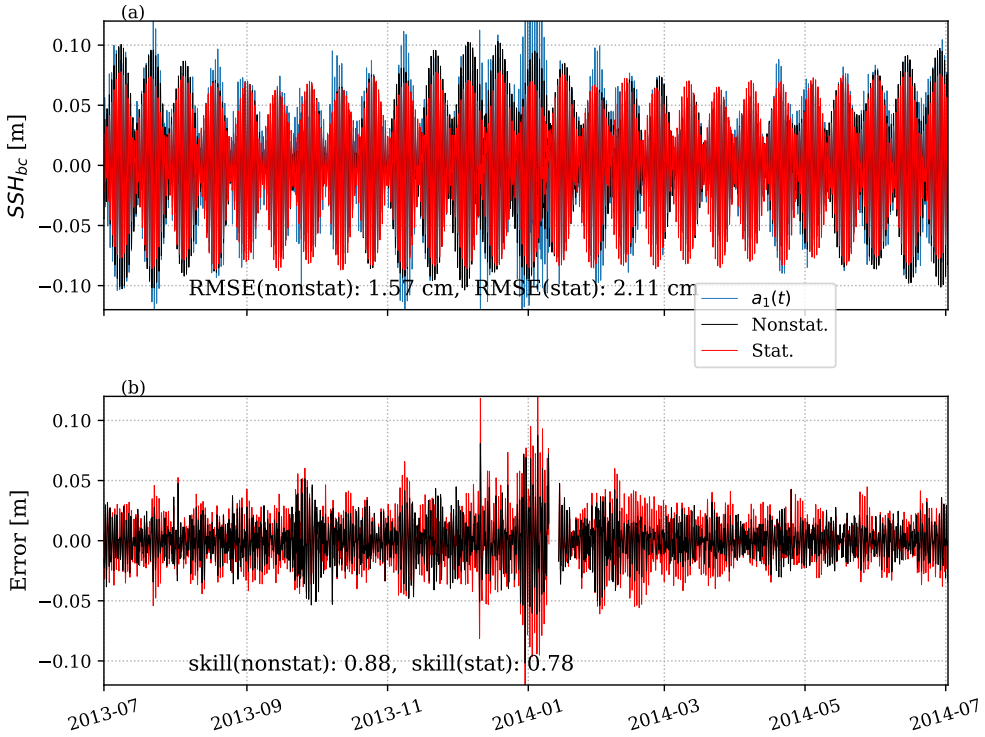

Figure 5. (Top) Baroclinic sea surface height perturbation (SSH_{BC}) at the ITFTIS mooring with the nonstationary (black) and stationary models (overlaid). (Bottom) Error (model-observed) for the nonstationary (black) and stationary (red) models.

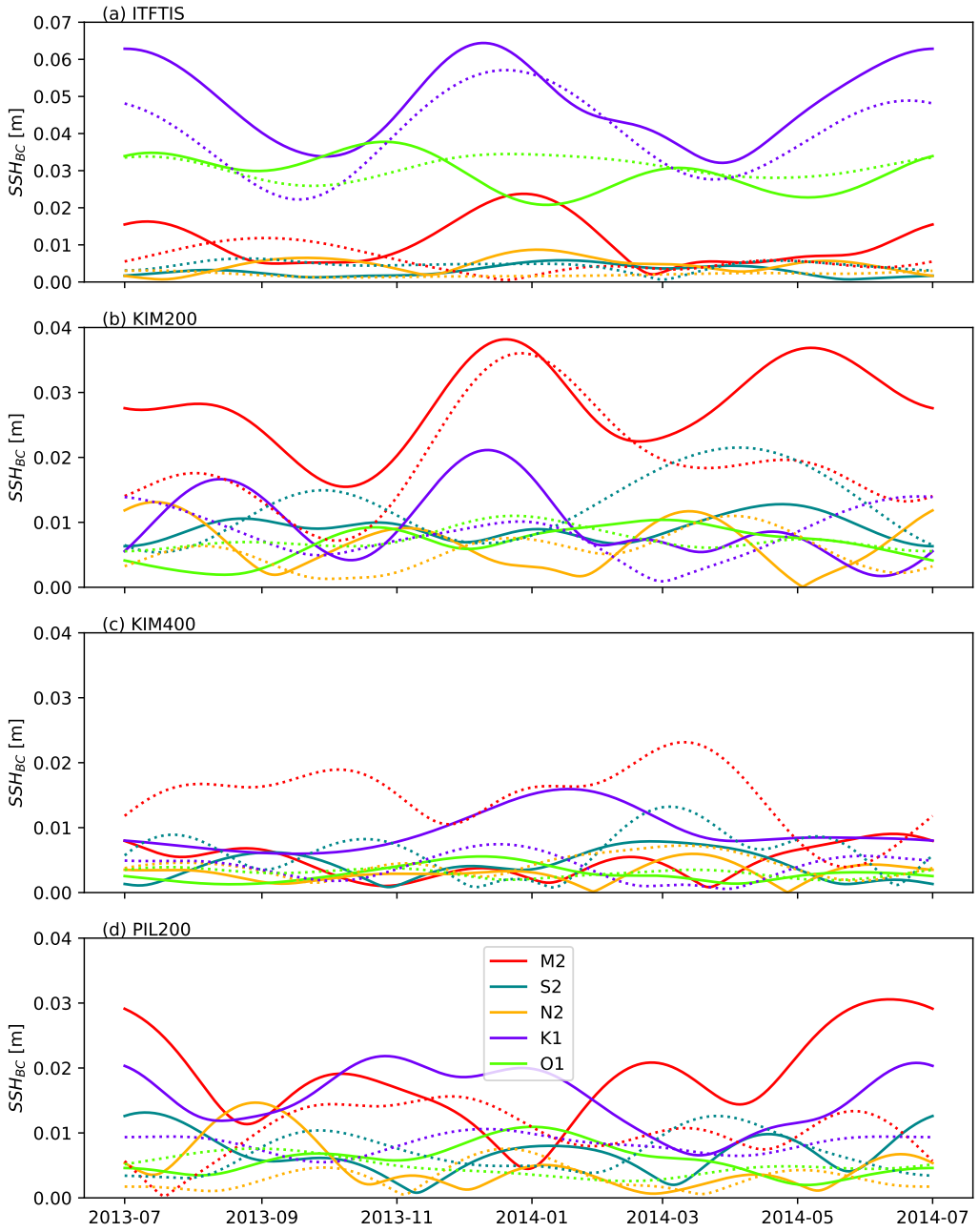

Figure 6. Seasonal modulation of $|\eta_m(t)|$ (Eq. 5) for each of the five primary tidal harmonics at (a) ITFTIS, (b) KIM200, (c) KIM400, and (d) PIL200 mooring locations. The solid lines in each panel indicate fits to the *in situ* data and dotted lines are the SUNTANS model data. Note the different vertical scale in (a).

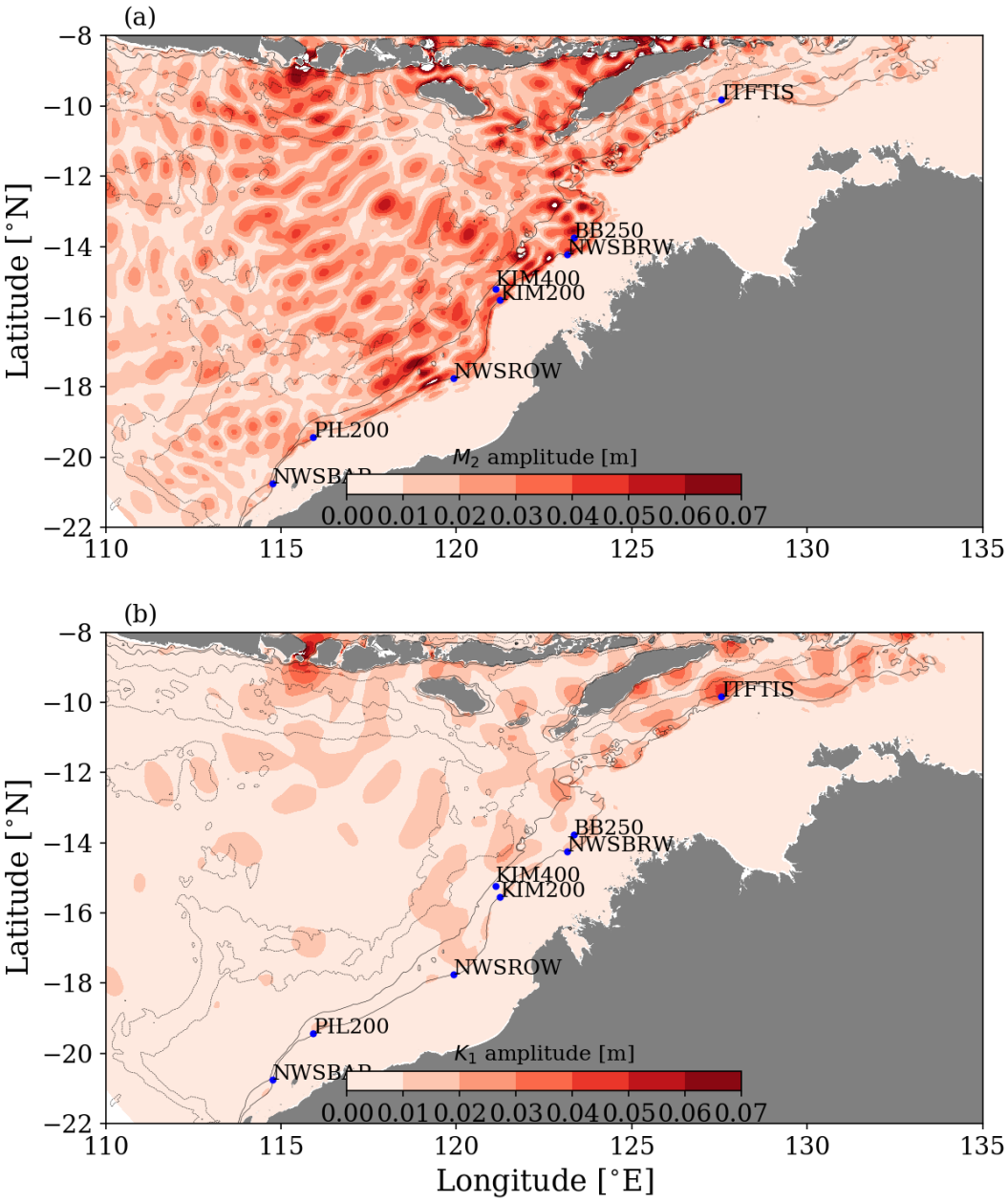

Figure 7. Mean baroclinic sea surface height harmonic amplitudes for (a) the M_2 and (b) the K_1 tidal constituents from the 12-month SUNTANS simulation.

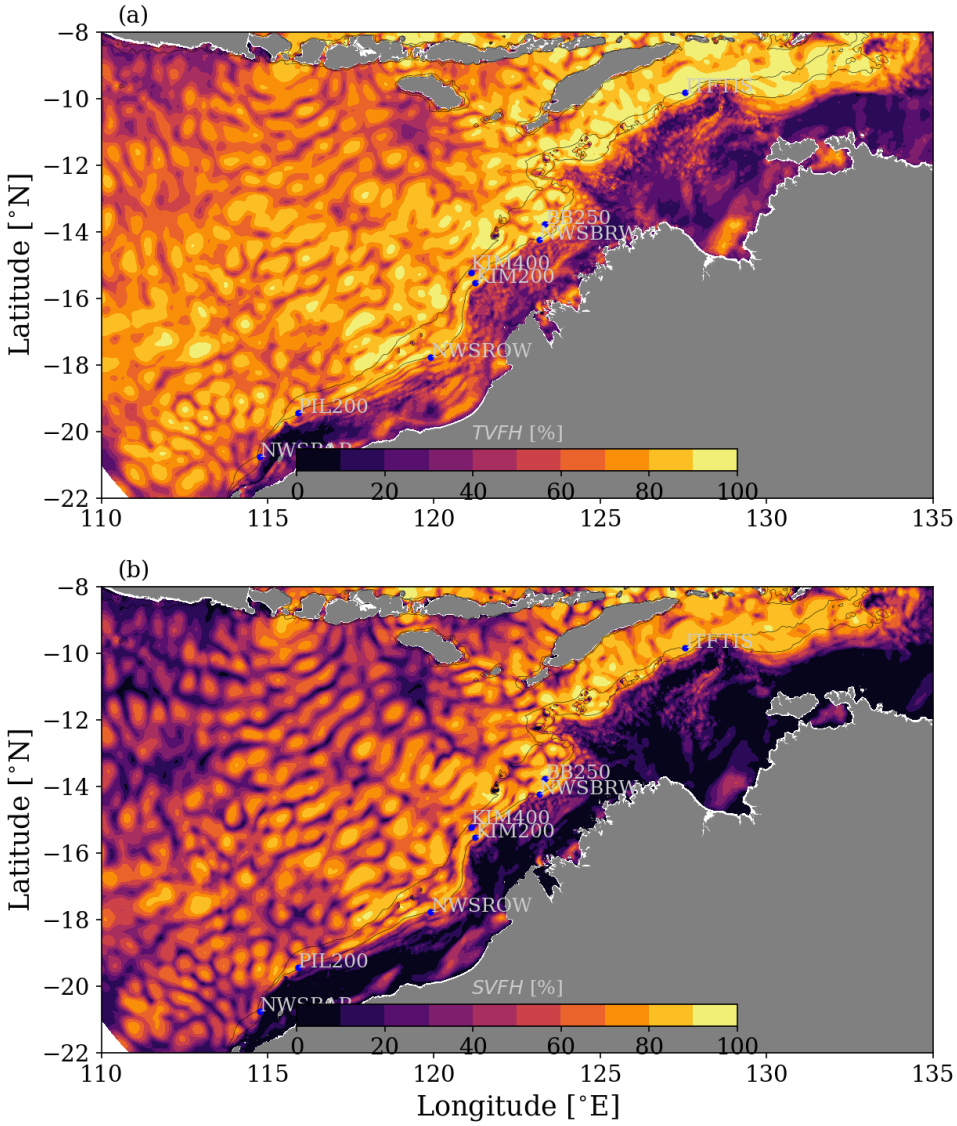

Figure 8. Percentage of variance of the SUNTANS baroclinic SSH (Eq. 8) explained by the (a) non-stationary (TVFH) and (b) stationary harmonic models (SVFH).

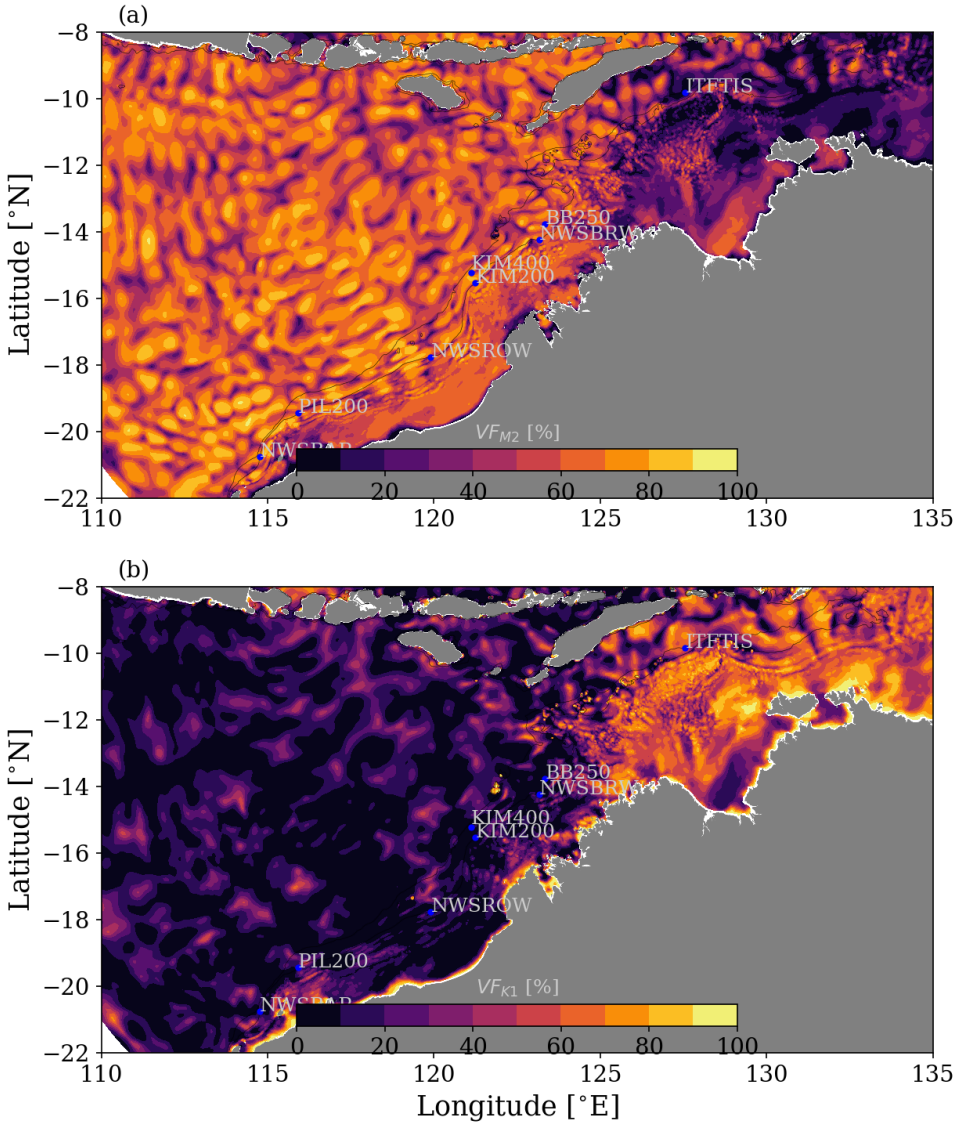

Figure 9. Percentage of variance of the SUNTANS baroclinic SSH (VF_m, Eq. 9) explained by the (a) M_2 and (b) K_1 band harmonics, i.e., including the non-stationary annual harmonics.

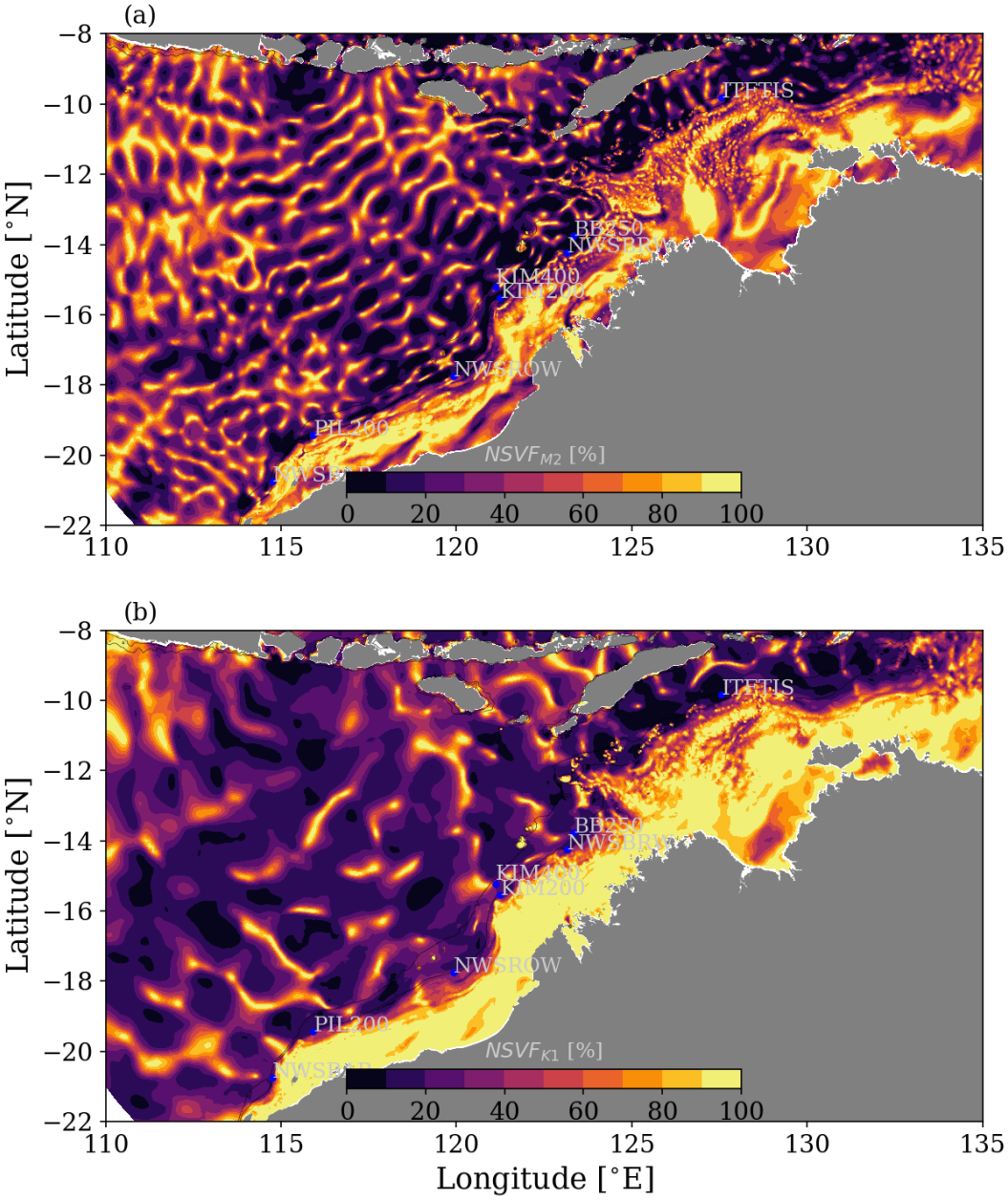

Figure 10. Percentage of variance of the SUNTANS baroclinic SSH ($NSVF_m$, Eq. 10) explained by the non-stationary harmonics in the (a) M_2 and (b) K_1 bands.

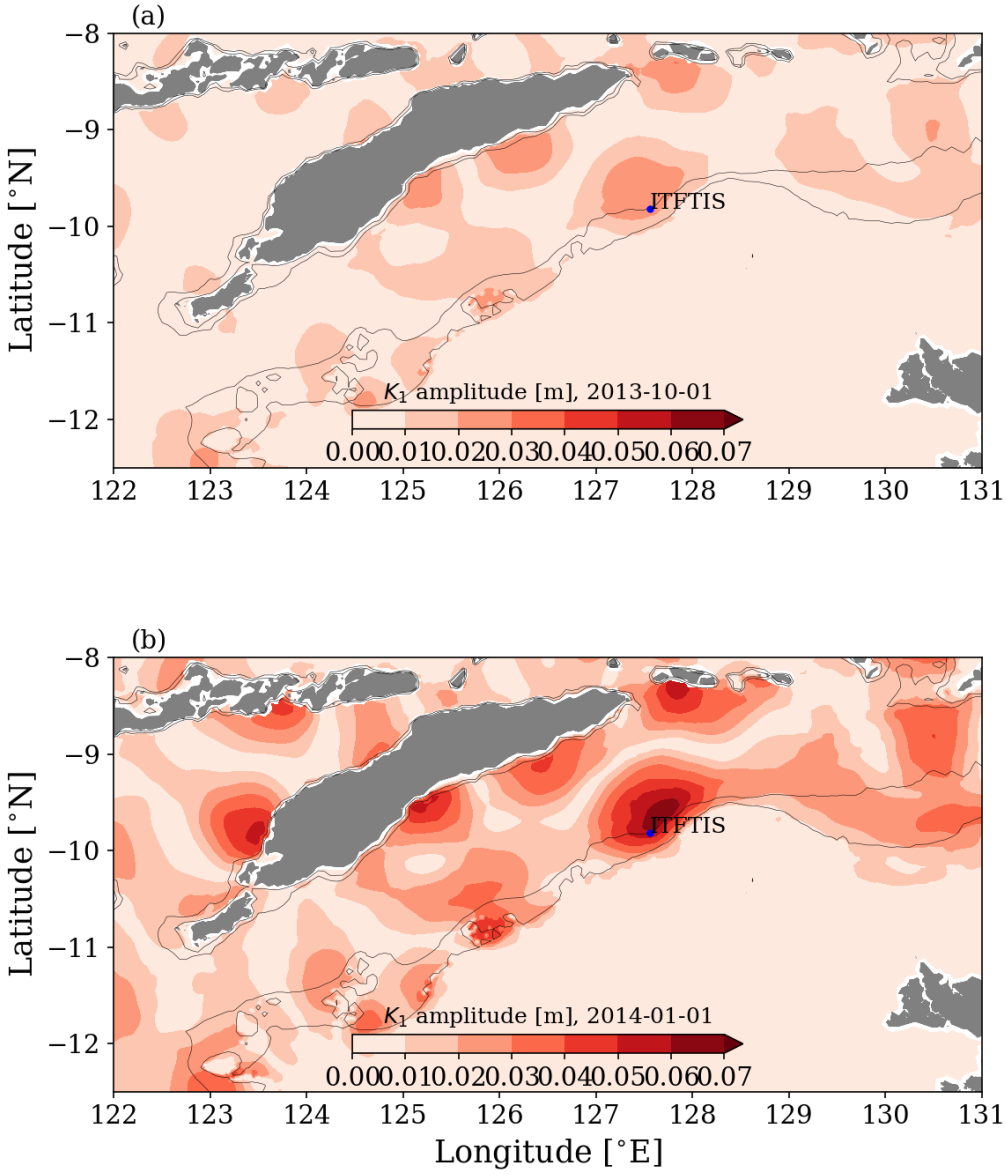

Figure 11. Snap-shots of $|\eta_{K1}(t)|$ from the Timor Sea region during October and January.

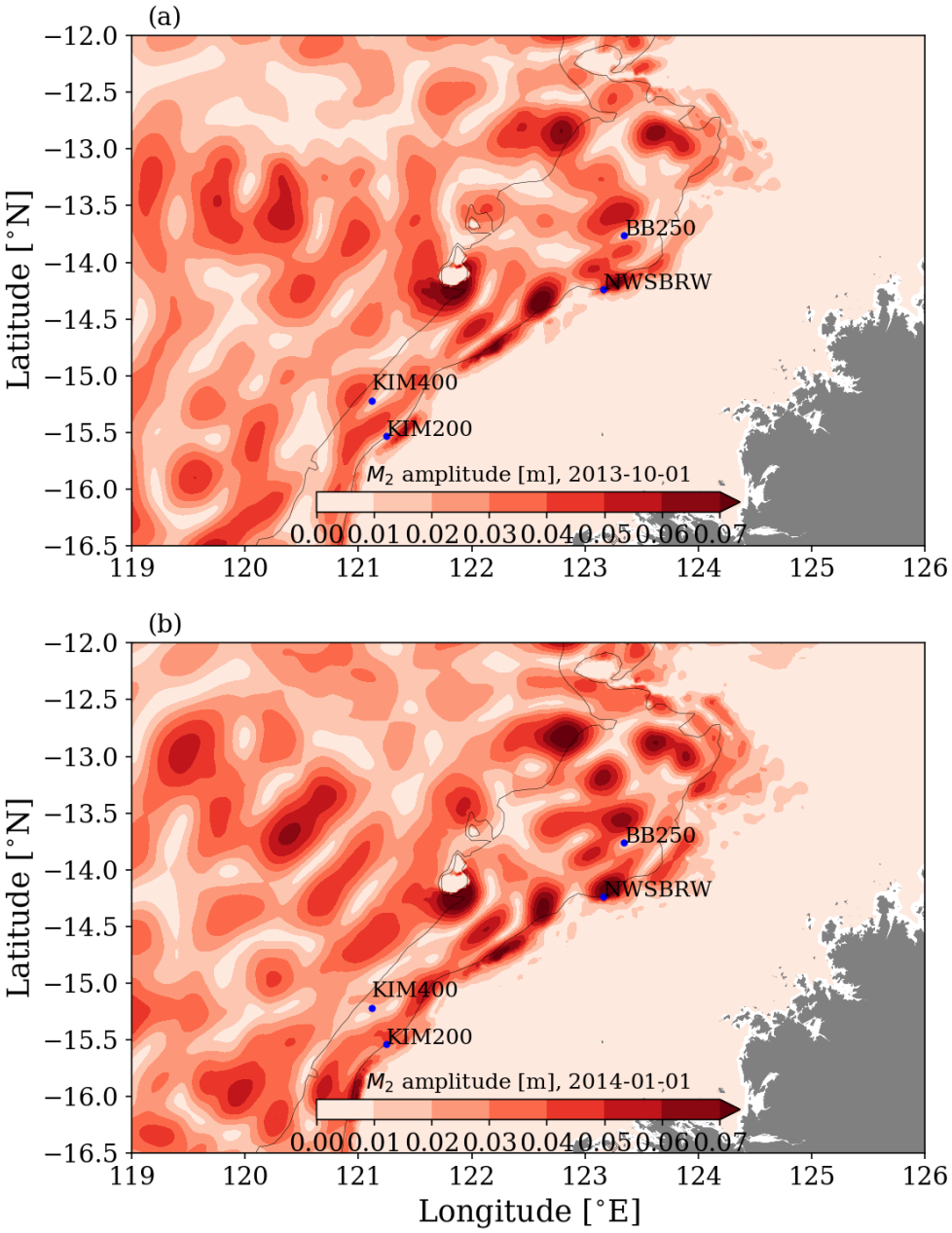

Figure 12. Snap-shots of $|\eta_{M2}(t)|$ from the Browse Basin region during October and January.

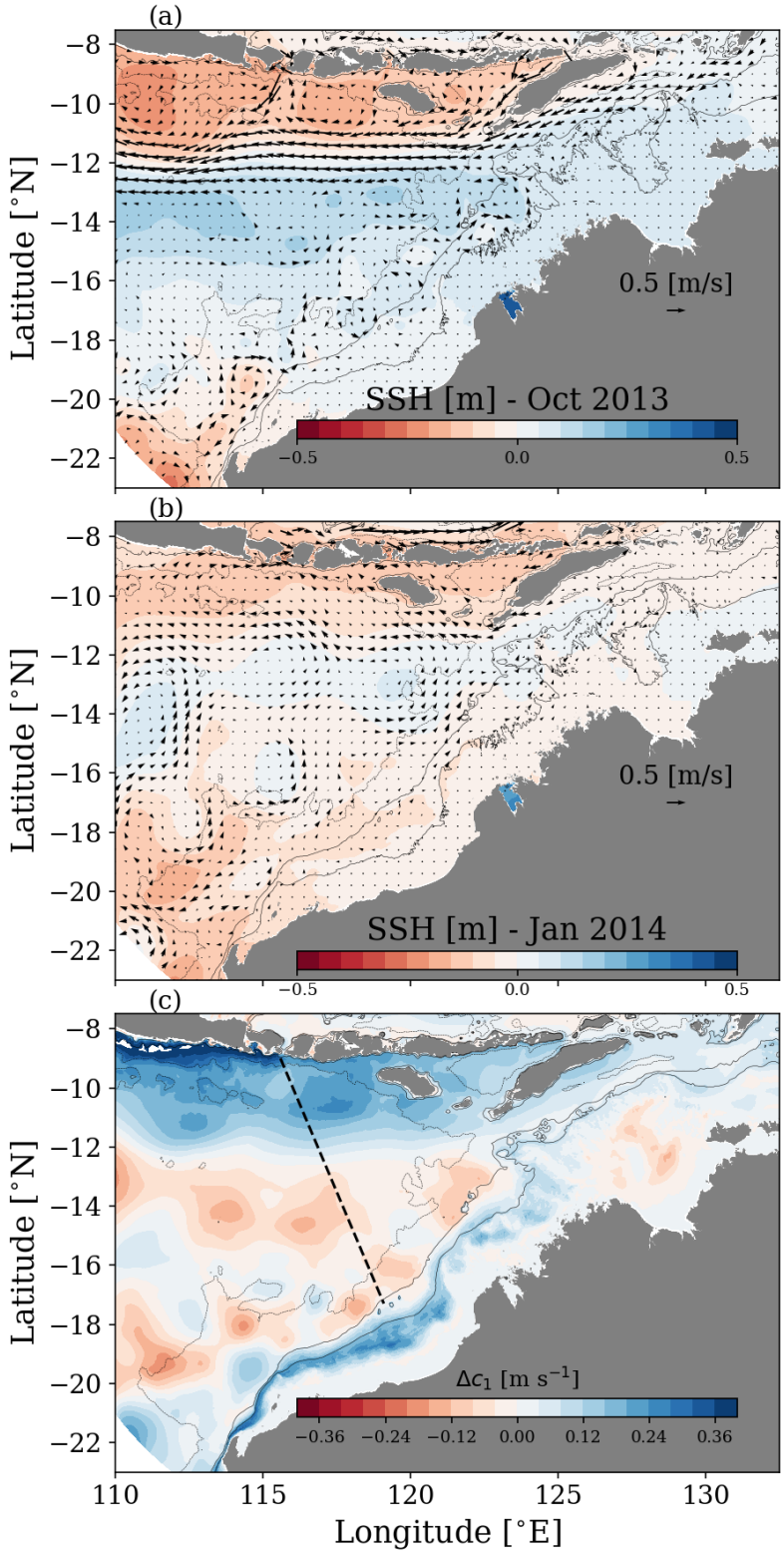

Figure 13. Monthly-averaged sea surface height (contours) and surface velocity (vectors) from the SUNTANS model for (a) October 2013 and (b) January 2014. The vector scale is indicated in the bottom right corner of each panel. (c) Indicates the mode-1 linear phase speed difference between the two months (January minus October).

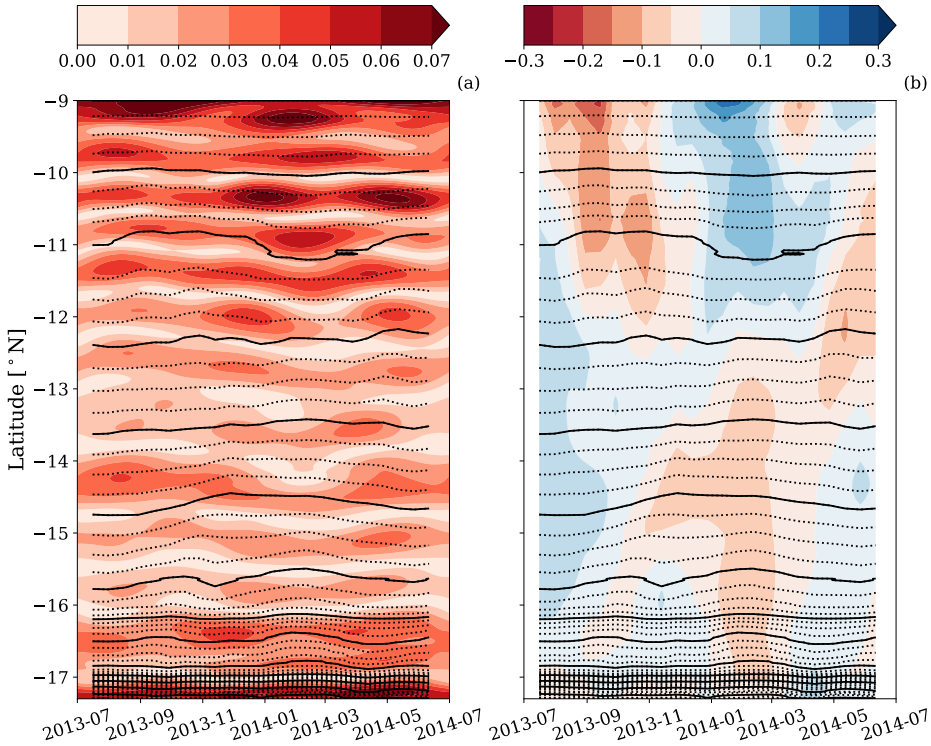

Figure 14. Temporal evolution of (a) $|\eta_{M2}|$ [m] and (b) mode-1 phase speed anomaly [m/s] along the transect in Fig. 13c. Black contours indicate an estimate of the propagation time from the northernmost point in one cycle intervals (dotted contours indicate quarter cycle intervals).

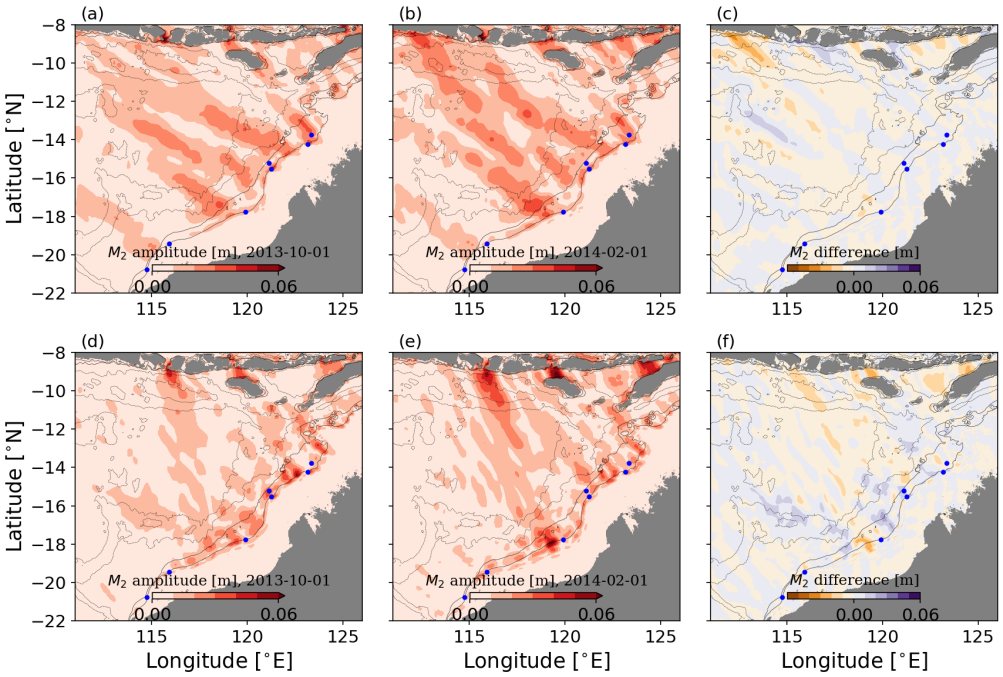

Figure 15. Directionally-decomposed internal tide sea surface height amplitude, $\eta_{M2}(t)$, for (a, d) October 2013 and (b, e) February 2014. The top row indicates the NW propagating portion of the signal, whereas the bottom row indicates the SE component. The last column shows the difference between October and February for (c) the NW and (f) the SE component.

935 ## Tables

Table 1. Details of each in situ mooring used in this study to measure through-water-column temperature.

Site ID	Location	Water Depth [m]	Deployment Period	No. Instruments
ITFTIS	Timor Sea	460	2010 - 2019	17
KIM200	Kimberley	200	Mar 2012 - Aug 2014	14
KIM400	Kimberley	405	Mar 2012 - Aug 2014	17
PIL200	Pilbara	202	Mar 2012 - Aug 2014	14
NWSBAR	Barrow Island	200	Aug 2019 - Feb 2020	15
NWSROW	Rowley Shoals	200	Aug 2019 - Feb 2020	14
NWSBRW	Browse Island	200	Aug 2019 - Feb 2020	15

Table 2. Statistics of the internal tide amplitude at each mooring. Standard deviation (Std. Dev.) and percentage of total mode-1 internal wave amplitude signal variance explained by two different band-pass filters: the internal tide filter (6 - 34 hour cutoff period) and the internal tide, including nonlinear steepening (3 - 34 hour cutoff).

		Percentage of Variance (%)	
Site	Std. Dev. [m]	6 - 34 hour	3 - 34 hour
ITFTIS	7.3	52.2	75.8
KIM200	6.5	30.0	80.5
KIM400	3.5	25.5	69.4
PIL200	7.1	28.3	77.0

Table 3. Performance metrics of the stationary (stat., Eq. 1) and nonstationary (nonstat., Eq. 6) models at predicting mode-1 internal tide amplitude at each of the mooring locations.

Site	RMSE [m] Stat.	RMSE [m] Nonstat.	Skill Stat.	Skill Nonstat.
ITFTIS	4.35	3.52	0.66	0.78
KIM200	3.62	2.90	0.70	0.81
KIM400	2.66	2.32	0.43	0.57
PIL200	4.72	4.19	0.45	0.57

Table 4. Performance metrics of the stationary (stat., Eq. 1) and nonstationary (nonstat., Eq. 6) models at predicting the sea surface height perturbation at each of the mooring locations for the period July 2013 - July 2014.

Site	RMSE [cm] Stat.	RMSE [cm] Nonstat.	Skill Stat.	Skill Nonstat.
ITFTIS	2.11	1.57	0.78	0.88
KIM200	1.91	1.6	0.56	0.69
KIM400	1.23	1.11	0.27	0.41
PIL200	2.41	2.14	0.30	0.45

Table 5. Performance metrics of the stationary (stat., Eq. 1) and nonstationary (nonstat., Eq. 6) models at predicting sea surface height perturbation at each of the mooring locations for the period when data was withheld (July 2012 - July 2013).

Site	RMSE [cm] Stat.	RMSE [cm] Nonstat.	Skill Stat.	Skill Nonstat.
ITFTIS	2.15	2.13	0.75	0.76
KIM200	2.13	2.16	0.46	0.45
KIM400	1.38	1.41	0.12	0.08
PIL200	3.08	3.04	0.16	0.18

Table 6. Validation metrics for the SUNTANS-derived SSH_{BC} from Eq. 6 compared against in situ observations.

Site	Dates	RMSE [cm]	Skill
ITFTIS	July 2013- Jun 2014	3.25	0.47
KIM200	July 2013- Jun 2014	2.29	0.37
KIM400	July 2013- Jun 2014	1.82	-0.60
PIL200	July 2013- Jun 2014	2.85	0.02
NWSBAR	Aug 2019 - Feb 2020	4.58	0.12
NWSROW	Aug 2019 - Feb 2020	2.86	0.45
NWSBRW	Aug 2019 - Feb 2020	5.80	0.67

Table 7. Description of different tidal harmonic metrics from the SUNTANS model at each in situ observation site.

Site	TVFH	SVFH	VF_M2	VF_K1	NSVF_M2	NSVF_K1
ITFTIS	94.7	87.2	2.1	61.8	40.3	9.5
KIM200	68.0	54.3	54.6	9.9	20.7	30.5
KIM400	49.7	28.5	67.2	6.8	40.4	36.4
PIL200	61.7	35.5	43.2	23.8	59.1	16.4
NWSBAR	68.4	58.3	76.9	11.9	10.4	23.2
NWSROW	75.7	62.8	36.6	8.0	14.0	28.1
NWSBRW	94.5	89.7	56.9	2.9	2.1	15.4